VALIDATION OF A SCALED PLANE STRAIN HYPERVELOCITY GOUGING MODEL

THESIS

Ronald J. Pendleton, Captain, USAF

AFIT/GAE/ENY/06-M26

DEPARTMENT OF THE AIR FORCE
AIR UNIVERSITY

AIR FORCE INSTITUTE OF TECHNOLOGY

Wright-Patterson Air Force Base, Ohio

APPROVED FOR PUBLIC RELEASE; DISTRIBUTION UNLIMITED

The views expressed in this thesis are those of the author and do not reflect the official policy or position of the United States Air Force, Department of Defense, or the U.S. Government.

AFIT/GAE/ENY/06-M26

VALIDATION OF A SCALED PLANE STRAIN HYPERVELOCITY GOUGING MODEL

THESIS

Presented to the Faculty

Department of Aeronautics and Astronautics

Graduate School of Engineering and Management

Air Force Institute of Technology

Air University

Air Education and Training Command

In Partial Fulfillment of the Requirements for the

Degree of Master of Science in Aeronautical Engineering

Ronald J. Pendleton, BS

Captain, USAF

March 2006

APPROVED FOR PUBLIC RELEASE; DISTRIBUTION UNLIMITED

AFIT/GAE/ENY/06-M26

VALIDATION OF A SCALED PLANE STRAIN HYPERVELOCITY GOUGING MODEL

Ronald J. Pendleton, BS

Captain, USAF

Approved:

Dr. Anthony N. Palazotto (Chair)	Date
Dr. Theodore Nicholas (Member)	Date
Dr. William P. Baker (Member)	Date

Abstract

The phenomenon of high speed impact is of great interest to the Air Force Office of Scientific Research and the Air Force Research Laboratory's Holloman High Speed Test Track. Rocket sled tests at the facility frequently are limited to velocities lower than actually attainable due to damage to the rail in the form of gouges. Direct observation of this gouging phenomenon is not currently possible. This leaves computational modeling as the only means to study the phenomenon. A computer model has previously been used to model the development of gouging at the Holloman High Speed Test Track. However, this model has not been experimentally verifiable due to its complexity.

This research is primarily concerned with comparing experiment and analysis of a simplified gouging model. This simplified gouging experiment utilized a 30 mm powder gun to shoot cylindrical projectiles at a target at oblique angles. Computer simulations of the event overestimated penetration depths by 13 to 29 percent, which is well within acceptable limits.

Using dimensional analysis, the simplified gouging model was scaled up to an equivalent sled system model. While this equivalent system does not actually exist, it does give reasonable estimates for similar sized systems.

Acknowledgements

I would like to express my sincere appreciation to my faculty advisor, Dr. Anthony N. Palazotto, for his guidance and support throughout the course of this thesis effort. The insight and experience was certainly appreciated. I would also like to thank the members of my thesis committee, Dr. William P. Baker and Dr. Theodore Nicholas, for their time and patience. Major John Cinnamon was instrumental in keeping the greater project on target. This research has been sponsored by the Air Force Office of Scientific Research with Dr. Neal D. Glassman as the program manager.

Ronald J Pendleton

Table of Contents

Page

Abstract iv
Acknowledgements v
Table of Contents vi
List of Figures viii
List of Tables x
I. Introduction 1
  Background 1
  Gouging Phenomenon 2
  Problem Statement and Objectives 4
II. Theory 5
  Conservation Equations 5
  Stress Waves in a Continuum 6
    Elastic Stress Waves. 7
    Plastic Stress Waves. 13
    Shock Waves. 16
  Constitutive Equation 21
  Equation of State 23
  Buckingham Pi Theorem 25
III. Methodology 27
  Cinnamon Experiments 28
  Model Development 32
    Rod Impact Model. 37
    Equivalent HHSTT Sled System. 39
  CTH Model and Solution Method 41
    Model Boundary Conditions. 43
    Axisymmetric – Plane Strain Comparison. 44
    Rod Impact Model. 46
IV. Analysis and Results 47
  Axisymmetric – Plane-Strain Comparison 47
    375 m/s Impact Velocity. 48
    555 m/s Impact Velocity. 54
  Rod Impact Simulation 60
    Test #1 Simulation, v=2225 m/s @ 10°. 61
    Test #4 Simulation, v=2163 m/s @ 10°. 63
    Test #2 Simulation, v=2150 m/s @ 15°. 65
    Test #3 Simulation, v=2147 m/s @ 15°. 68
  Equivalent HHSTT Sled System 70
V. Conclusions and Recommendations 73
  Conclusions 73
  Recommendations for Future Research 74
Appendix A. CTH Input Deck of Axisymmetric – Plane Strain Comparison 76
Appendix B. CTH Input Deck for Rod Impact Test #1 80

Page
Appendix C. CTH Plots of Cinnamon Simulations.....85
Bibliography 86

List of Figures

Page

Figure 1 – HHSTT Rocket Sled 2
Figure 2 – Rail/Slipper Configuration 2
Figure 3 – Rail Gouge 3
Figure 4 – Gouge Illustration [2] 4
Figure 5 – Rod Impact Experiment 7
Figure 6 – Material Element 9
Figure 7 – Rod Impact Experiment 11
Figure 8 – Rod Impact Before Reflection 11
Figure 9 – Rod Impact at Reflection 12
Figure 10 – Rod Impact After Reflection 12
Figure 11 – Rod Impact After Unloading 13
Figure 12 – Bilinear Stress-Strain Curve and Corresponding Wave Profile 14
Figure 13 – Concave-up Stress-Strain Curve 15
Figure 14 – Shock Formation 15
Figure 15 – Conditions at a Shock Front [7] 16
Figure 16 – Hugoniot Curve Showing Loading and Unloading Paths [7] 20
Figure 17 – 30 mm Powder Gun 28
Figure 18 – Experimental Target Area 29
Figure 19 – Experimental Target 29
Figure 20 – Experimental Test 1 Gouge 30
Figure 21 – Experimental Test 2 Gouge 30
Figure 22 –Target Rail for Tests 3 and 4, Before Test 31
Figure 23 – Experimental Test 3 Gouge 31
Figure 24 – Experimental Test 4 Gouge 31
Figure 25 – HHSTT Sled Simplification 33
Figure 26 – Rod Impact Model 38
Figure 27 – Rod Impact and Equivalent HHSTT Model Comparison 40
Figure 28 – Vertical Impact for Axisymmetric – Plane Strain Comparison 45
Figure 29 – Vertical Impact Mesh 45
Figure 30 – Rod Impact Model Mesh 46
Figure 31 – Axisymmetric and Plane-Strain Comparison (t = 0 s) 48
Figure 32 - v = 375, axi, t=2.5 μs
Figure 33 - v = 375, pl st, t=2.5 μs 49
Figure 34 - v = 375, axi, t=7.5 μs
Figure 35 - v = 375, pl st, t=7.5 μs 49
Figure 36 - v = 375, axi, t=10.0 μs
Figure 37 - v = 375, pl st, t=10.0 μs 50
Figure 38 - v = 375, axi, t=12.0 μs
Figure 39 - v = 375, pl st, t=12.0 μs 50
Figure 40 – TP 1 y Position, axi
Figure 41 – TP 1 y Position, pl st 51
Figure 42 – TP 3 y Position, axi
Figure 43 – TP 3 y Position, pl st 52
Figure 44 – Pressure, axi, t=1.5 μs
Figure 45 – Pressure, pl st, t=1.5 μs 52
Figure 46 – Pressure, axi, t=5.0 μs
Figure 47 – Pressure, pl st, t=5.0 μs 53
Figure 48 – Pressure, axi, t=10.0 μs
Figure 49 – Pressure, pl st, t=10.0 μs 53
Figure 50 – v = 555, axi, t=2.0 μs
Figure 51 – v = 555, pl st, t=2.0 μs 54

Page

Figure 52 – v = 555, axi, t=6.0 μs Figure 53 – v = 555, pl st, t=6.0 μs 55
Figure 54 – v = 555, axi, t=8.0 μs Figure 55 – v = 555, pl st, t=8.0 μs 55
Figure 56 – v = 555, axi, t=10.0 μs Figure 57 – v = 555, pl st, t=10.0 μs 56
Figure 58 – TP 1 y Position, axi Figure 59 – TP 1 y Position, pl st 57
Figure 60 – TP 3 y Position, axi Figure 61 – TP 3 y Position, pl st 58
Figure 62 – Pressure, axi, t=1.5 μs Figure 63 – Pressure, pl st, t=1.5 μs 58
Figure 64 – Pressure, axi, t=5.0 μs Figure 65 – Pressure, pl st, t=5.0 μs 59
Figure 66 – Pressure, axi, t=10.0 μs Figure 67 – Pressure, pl st, t=10.0 μs 59
Figure 68 – CTH Rod Impact Model, (t = 0 s) 61
Figure 69 – Test #1 Sim, t=3.0 μs Figure 70 – Test #1 Sim, t=4.5 μs 61
Figure 71 – Test #1 Sim, t=6.5 μs Figure 72 – Test #1 Sim, t=10.0 μs 62
Figure 73 – Test #1 Sim, t=10 μs, zoom 62
Figure 74 – Test #1 Pressure Profile, t=10.0 μs Figure 75 – Test #1 Strain Rate, t=10.0 μs 63
Figure 76 – Test #4 Sim, t=3.0 μs Figure 77 – Test #4 Sim, t=4.5 μs 64
Figure 78 – Test #4 Sim, t=6.5 μs Figure 79 – Test #4 Sim, t=10.0 μs 64
Figure 80 – Test #4 Sim, t=10.0 μs 65
Figure 81 – Test #2 Sim, t=2.5 μs Figure 82 – Test #2 Sim, t=5.5 μs 66
Figure 83 – Test #2 Sim, t=10.0 μs 66
Figure 84 – Test #2 Sim, t=10.0 μs 67
Figure 85 – Test #2 Pressure Profile, t=10.0 μs Figure 86 – Test #2 Strain Rate, t=10.0 μs 67
Figure 87 – Test #3 Sim, t=2.5 μs Figure 88 – Test #3 Sim, t=5.5 μs 68
Figure 89 – Test #3 Sim, t=10.0 μs 68
Figure 90 – Test #3 Sim, t=10.0 μs 69
Figure 91 - Equivalent Model, t=10 μs Figure 92 – Pressure, Equivalent Model, t=10 μs 71
Figure 93 – Strain-Rate, Equivalent Model, t=10 μs 72
Figure 94 – Equivalent HHSTT Model, t=10 μs 72

List of Tables

Page
Table 1 – Cinnamon Experiment Results 32
Table 2 – Buckingham Pi Input Variables 33
Table 3 – Buckingham Pi Variable Selection Changes 34
Table 4 – Buckingham Pi Dimensioned Quantities 35
Table 5 – Rod Impact Projectile Properties 38
Table 6 – Rod Impact Model Parameters 38
Table 7 – Typical HHSTT Sled System Quantities 40
Table 8 – Johnson-Cook Coefficients 43
Table 9 – Pressure Difference, v = 375 m/s 54
Table 10 – Pressure Difference, v = 555 m/s 60
Table 11 – Time Range Comparison 60
Table 12 – Comparison of Experimental and CTH Results 70
Table 13 – Model Comparison 70

VALIDATION OF A SCALED PLANE STRAIN HYPERVELOCITY GOUGING MODEL

I. Introduction

Background

The United States Air Force (USAF) owns and operates a high speed test track facility at Holloman Air Force Base in New Mexico where they can test various hardware systems in simulated free flight conditions. The system consists of a rocket powered sled that glides on railroad track like rails as shown in Figure 1. The high velocity track has a narrow gauge and is just shy of ten miles long. The Holloman High Speed Test Track (HHSTT) is operated by the 846th Test Squadron. In 2003, they set a world land speed record of 2884.9 m/s. They would like to increase the speed to above Mach 10 (~3000 m/s). In the past, the HHSTT has experienced serious problems with rail damage from a test run. The 846th Test Squadron and the Air Force Institute of Technology (AFIT) are investigating methods of understanding this phenomenon known as gouging in order to mitigate the damage.

Figure 1 – HHSTT Rocket Sled

Gouging Phenomenon

The rocket sled is attached to the rails via four slippers. The rail/slipper configuration is shown in Figure 2. The rail material is 1080 steel, while the slipper is VascoMax 300 (a high strength steel).

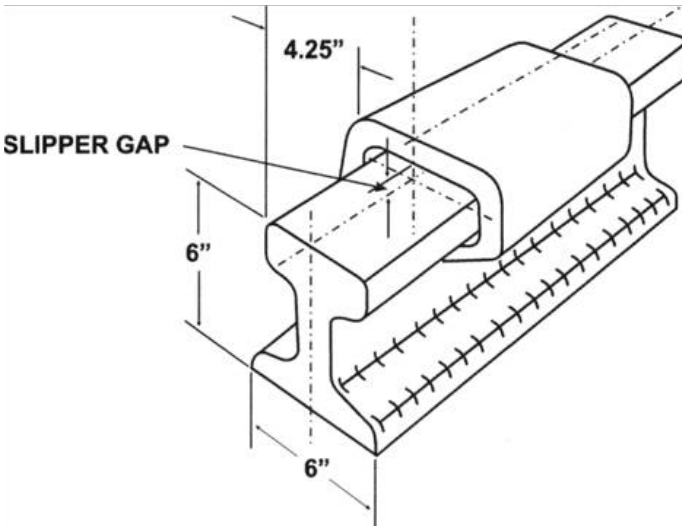

Figure 2 – Rail/Slipper Configuration

Gouging at the HHSTT typically occurs at velocities greater than 1.5 km/s. Hooser [1] found the vertical velocity to be on the order of 1-2 m/s with a 1.5 km/s horizontal velocity. This shows that the slipper impinges the rail with an angle of approximately 0.03°. The resulting damage can range from minor gouges as shown in

Figure 3 to total structural failure. The test sled slippers disintegrate upon impact at the end of the track and are not recoverable for analysis.

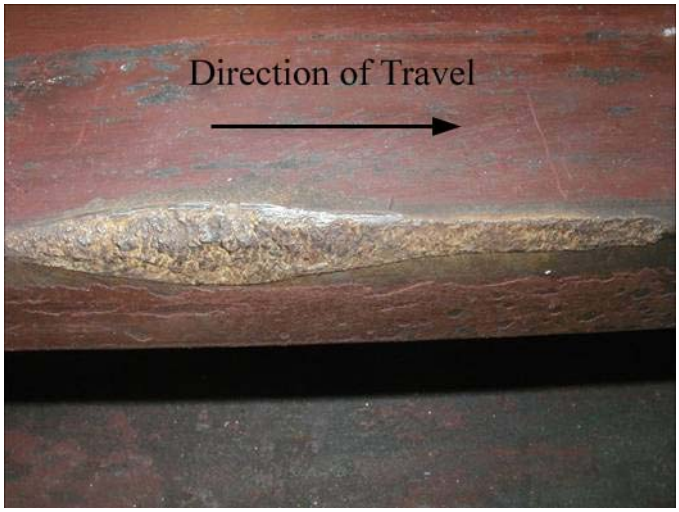

Figure 3 – Rail Gouge

Laird [2; 3] was one of the first to investigate and define gouging for the HHSTT. Gouging occurs when inertial forces are so great that the materials exhibit fluid like behavior. The relative motion of the bodies deforms the material that continuously impinges on each other. The resulting plastic flow takes the form of material jets which continually grow and penetrate further into the two surfaces, initiating a gouge as shown illustratively in Figure 4.

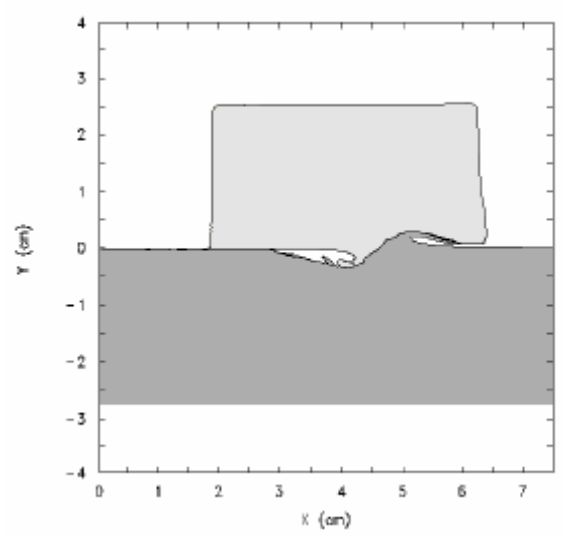

Figure 4 – Gouge Illustration [2]

Problem Statement and Objectives

Laird and Szmerekovsky [4; 5] studied the HHSTT slipper and rail interactions analytically using CTH, a hydrocode developed by Sandia National Labs. Szmerekovsky used the actual test sled conditions to perform his analysis. Because of this, his model is accepted as the standard simulation of the gouging phenomenon. Rickerd [6] developed a simplified gouging model equivalent to the Szmerekovsky model and simulated the gouging phenomenon with an oblique ballistic impact using CTH. Unfortunately, this simplified model requires velocities currently beyond the capabilities of test facilities here at AFRL. This research attempts to compare experiment and analysis of a gouging model that is possible here at AFIT. This model will then be scaled up to an equivalent HHSTT sled system.

II. Theory

Conservation Equations

The conservation equations are equations that express of the laws of physics. These equations are useful for problems involving time dependant high loading. In particular, when velocities or deformations of the structure are large. Virtually all fields of mechanics and dynamics are based on these fundamental principals:

(i) Mass is neither created nor destroyed: "conservation of mass"

(ii) Rate of change of momentum = Net force: "conservation of momentum"

(iii) Energy is conserved, though it may change form: "conservation of energy"

Mathematically, the conservation of mass is stated

$$\int_V \rho dV = constant \tag{1}$$

where ρ is density and V is the volume of the material.

The conservation of momentum can be stated in a number of different ways. Here mass is assumed to remain constant. This leads to force equals mass times acceleration, or

$$F = m\frac{dv}{dt} \tag{2}$$

where F is the force applied, m is the mass acted upon, v is the velocity of the mass, and t is the time over which the event occurs. Another useful statement of the conservation of momentum is the impulse-momentum relation, which is obtained by multiplying both

sides of the conservation of momentum equation by *dt* and integrating over a period of time, giving

$$I = \int F dt = \int m dv = m v_f - m v_o \qquad (3)$$

Where I is the impulse applied over some period of time by the applied force, v_f and v_o are the initial and final velocities of the mass, and therefore the right hand side of the equation is the momentum change over some time period.

Lastly, the conservation of energy equation written for a discrete set of *j* masses is

$$\sum_j \left(E_o + \frac{1}{2} \rho v_o^2 \right) = \sum_j \left(E_1 + \frac{1}{2} \rho v_1^2 \right) + W_{0 \to 1} \qquad (4)$$

where E is the internal energy source, the $\frac{1}{2} \rho v^2$ terms are kinetic energy. $W_{0 \to 1}$ is the work done on the system from the initial state, 0, to the final state, 1 [7].

Stress Waves in a Continuum

When pressure or load is applied to a material, stress waves develop and propagate within that material. In continuum mechanics, this fact is often ignored and the loading is said to be either static or quasi-static. This practice works well in most structural analysis problems where pressure or loads are applied very slowly, but in high velocity impact dynamics problems, is a poor simplification of what actually occurs. As the affected particles accelerate, they build up compressive stresses in the particles further from the application point. The motion of these particles is governed by the conservation of momentum. The speed of propagation of the stress wave, however, will be shown to be a material property.

In the following subsections, three regimes of dynamic impact will be described to understand the effects of impact velocities on stress wave propagation. In the first regime, elastic waves are formed by low velocity impacts. In the second regime higher velocities cause both an elastic wave and a plastic wave to form. The plastic wave trails the elastic wave and will cause permanent plastic deformation in portions of the material. In the third regime the impact velocity is much greater than the sound speed of the material which causes a narrow region of discontinuity in state properties.

Elastic Stress Waves.

It is possible to calculate the elastic stress wave in a uniaxial rod impact experiment. Figure 5 shows an initially stationary rod is impacted by a rigid, semi-infinite plate moving from left to right with constant velocity v_o, which is less than the material sound speed c. After the impact, an elastic stress wave travels to the right at the material sound speed, no matter what the impact velocity is.

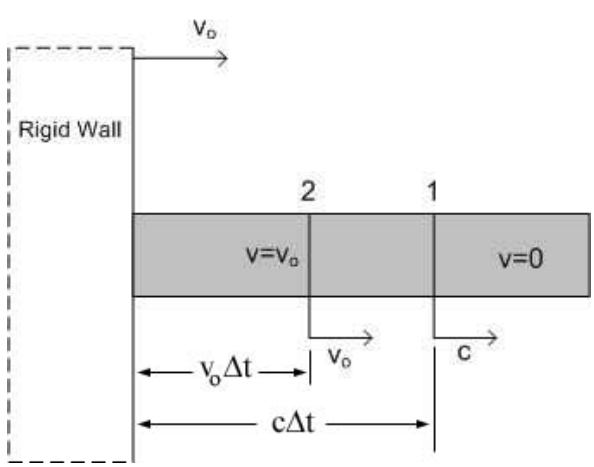

Figure 5 – Rod Impact Experiment

Behind the stress wave, location 1, the material particles have been accelerated to a velocity equal to the impact velocity v_o. The momentum of that material is

$$\rho A c \Delta t v_o \tag{5}$$

Where ρ is the density of the material, $c\Delta t$ is the length of the rod which is moving with a particle velocity of v_o, and A is the cross sectional area of the rod. $v_o\Delta t$ is the actual deformation imposed.

With the momentum defined, an expression for the impulse acting on the material is needed to define the elastic stress wave. From basic physics, the impulse is known to be the integral of the force over a period of time. In the uniaxial case, the force is the stress times the area over which it acts, giving an impulse of

$$\sigma A dt \tag{6}$$

where σ is the compressive stress at any point in the bar occurring due to the passage of the stress wave. The elastic compressive stress wave is obtained by applying the conservation of momentum to Equations 5 and 6, assuming an infinitesimal time step, and dividing both sides by the area and time step. The result is

$$\sigma = \rho c v_o \tag{7}$$

where c is the material sound speed.

The rod impact case allows the material sound speed to be determined. From the rod, an infinitesimal element of area A experiences the passage of a disturbance, as shown in Figure 6.

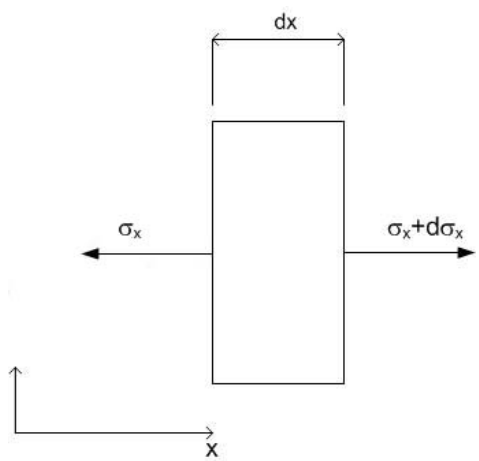

Figure 6 – Material Element

The left and right edges of the element are at positions of x and $x + dx$, respectively. Assuming positive tension in the positive x direction, the stress on the left and right sides of the element are

$$-\sigma_x \quad \textbf{and} \quad \sigma_x + \frac{\partial \sigma_x}{\partial x}, \tag{8}$$

respectively. The conservation of momentum for the infinitesimal element is given by

$$A(-\sigma_x)dt + A\left(\sigma_x + \frac{\partial \sigma_x}{\partial x}\right)dt = (\rho A)dv \tag{9}$$

where the left hand side of the equation is the impulse applied due to the stress on the left and right boundaries, and the right hand side of the equation is the momentum imparted over the differential time step. Dividing both sides by Adt gives

$$\frac{\partial \sigma_x}{\partial x} = \rho \frac{dv}{dt}. \tag{10}$$

Using one dimensional strain and velocity,

$$\varepsilon = \frac{\partial u}{\partial x} \quad \textbf{and} \quad v = \frac{\partial u}{\partial t}, \tag{11}$$

it can be shown that

$$\frac{\partial \varepsilon}{\partial t} = \frac{\partial v}{\partial x}. \tag{12}$$

If stress is assumed to be only a function of strain, then Equations 10 and 12 can be combined to give the uniaxial wave equation,

$$c^2 \frac{\partial^2 u}{\partial x^2} = \frac{\partial^2 u}{\partial t^2} \tag{13}$$

where

$$c^2(\varepsilon) = \frac{d\sigma / d\varepsilon}{\rho}. \tag{14}$$

For elastic behavior, the numerator is the elastic modulus. This gives the bulk sound wave velocity for a uniaxial stress elastic impact as,

$$c = \sqrt{\frac{E_m}{\rho}} \tag{15}$$

where E_m is the elastic modulus and ρ is the density. For uniaxial strain (plane strain), the bulk sound wave velocity is

$$c = \sqrt{\frac{E_m(1-\nu)}{\rho(1+\nu)(1-2\nu)}} \tag{16}$$

where ν is the Poisson's ratio [7] .

Understanding how waves propagate through a medium and what happens at the boundaries will be important in analyzing stress waves in subsequent sections. Again assuming a uniaxial homogeneous metal rod impacting a semi-infinite rigid wall at a

velocity of v_o perpendicular to the wall as in Figure 7. Because the impact is perpendicular and uniaxial, it is assumed that there are no three-dimensional effects. It is also assumed that the impact is completely elastic and that the wave velocity within the rod is constant. The rod is moving to the left at a uniform velocity of v_o and has zero stress before impact. At the moment of impact $t = t_o$.

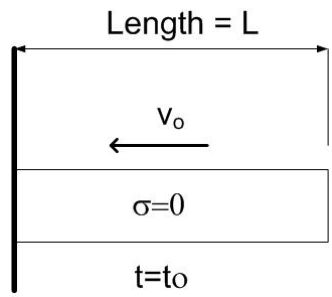

Figure 7 – Rod Impact Experiment

After impact ($t_o < t < L/c$), a stress wave propagates to the right at the material sound speed as shown in Figure 8. Particles to the left of the wave experience a constant compressive stress as described by Equation 7 and due to continuity at the left boundary (fixed), the rod velocity must be zero. To the right of the stress wave the rod continues to travel to the left at the initial velocity v_o because the right side hasn't "felt" the impact yet. The material sound speed limits how fast a disturbance can propagate throughout the material.

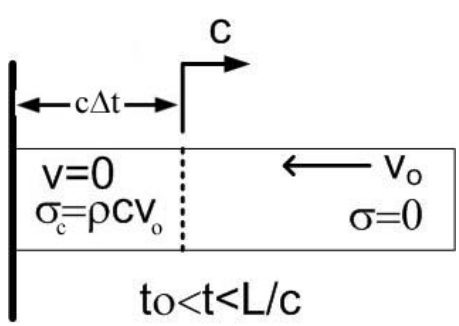

Figure 8 – Rod Impact Before Reflection

At $t = L/c$, the stress wave has reached the right end of the rod, see Figure 9. At this point the entire rod has zero velocity and is under constant compressive stress defined by Equation 7. Conservation of energy dictates that the kinetic energy of the rod before impact be converted into internal strain energy.

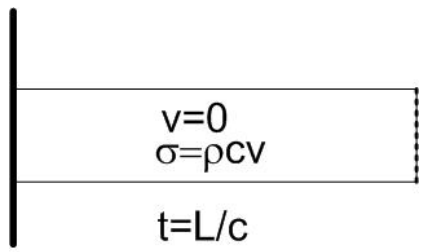

Figure 9 – Rod Impact at Reflection

From any mechanics of materials textbook it is known that a free surface, by definition, cannot support an applied stress. The only mechanism that can exist is a reflection of the stress wave, due to the free end. A stress wave is set up, opposite in sign but equal in magnitude, reducing the compressive stress. After reflection, ($L/c < t < 2L/c$), the right side of the stress wave must have zero stress, see Figure 10. Conservation of energy dictates that the internal strain energy be converted back to kinetic energy, and therefore, it's initial velocity v_o, but to the right. As the stress wave reflects from the free surface, it reflects with opposite sign (tension). This tension wave acts as an unloading wave, cancelling the effects of the incident compression wave.

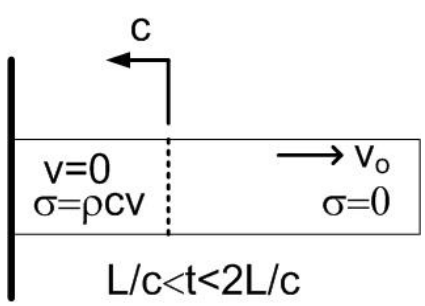

Figure 10 – Rod Impact After Reflection

At $t = 2L/c$, the stress wave is back at the left end of the rod attempting to apply a tensile stress to the rigid wall. Since the tensile stress can't be supported by the interface, the rod then separates from the wall. It rebounds off the wall, unstressed, at the initial velocity v_o, Figure 11.

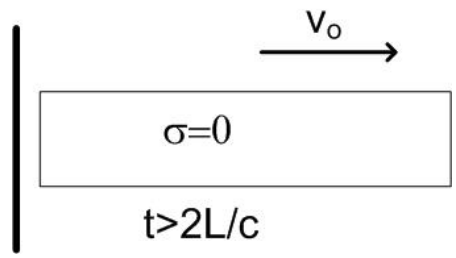

Figure 11 – Rod Impact After Unloading

Plastic Stress Waves.

For most metals, the stress-strain curve is characterized by a linear elastic region at low strains followed by a region that may or may not be linear as well. When a metal is loaded beyond the linear portion it will become permanently deformed. This transition point is known as the elastic limit, dynamic yield stress, or Hugoniot elastic limit [7]. In an impact experiment where the velocity is great enough to generate a stress higher than this limit, the initial stress wave is an elastic stress wave which is followed by a plastic stress wave.

There are two basic theories for describing plastic waves, the rate-independent theory and the rate-dependent theory. Both are uniaxial stress and as the names imply, the theories differ in their assumption of the importance of strain rate. The rate-independent theory assumes that there is a single stress-strain curve that describes material behavior and that a material had a bilinear stress-strain curve which doesn't depend on strain rate. The elastic stress wave would travel at the elastic sound speed

given earlier as, $c = \sqrt{\frac{E_m}{\rho}}$, and have a magnitude equal to $\sigma = \rho c v_o$. As stated earlier, for uniaxial stress, the plastic wave would have a slower velocity of,

$$c_p = \sqrt{\frac{E_p}{\rho}} \tag{17}$$

where E_p is the slope of the stress-strain curve in the plastic region and c_p is the plastic wave velocity. The magnitude of the stress wave would then be

$$\sigma_p = \rho c_p v_o \tag{18}$$

where σ_p is the plastic stress wave magnitude. Figure 12 shows a bilinear stress-strain curve and the corresponding wave profile.

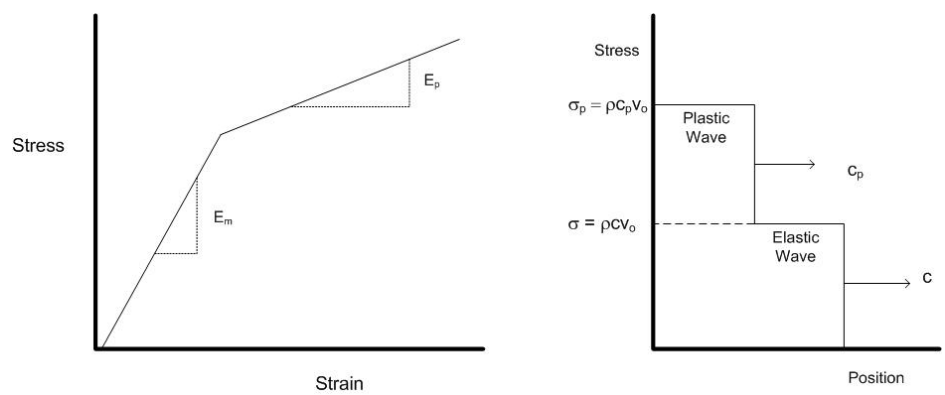

Figure 12 – Bilinear Stress-Strain Curve and Corresponding Wave Profile

An alternative analysis of the rate-independent theory assumes that the stress-strain curve is concave-up beyond the yield stress instead of linear, as in Figure 13. This generally occurs in states of uniaxial strain such as plate impact experiments. Uniaxial stress stress-strain curves are normally concave-down.

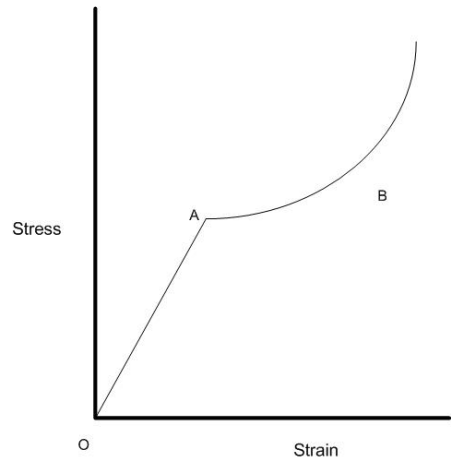

Figure 13 – Concave-up Stress-Strain Curve

As the strain is increased beyond the yield limit, the slope of the stress-strain curve, and therefore the velocity of the stress wave increases. This means that the higher stress waves will eventually overtake the low stress waves. At which point a plastic shock front is formed, as shown in Figure 14 [8].

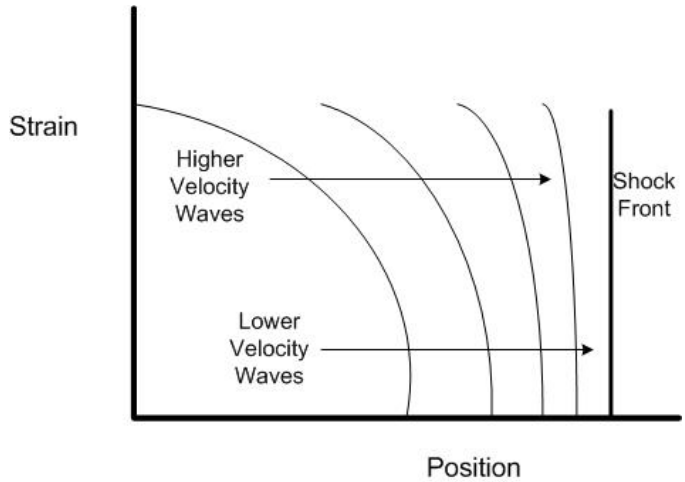

Figure 14 – Shock Formation

The rate-dependent theory was developed to account for strain rate dependence in plastic flow. This theory more accurately approximates the plastic stress-strain region. The most popular form involves an overstress model and is of the form

$$\sigma = f(\varepsilon) + \ln\left(1 + b\dot{\varepsilon}_p\right) \tag{19}$$

where $f(\varepsilon)$ is the stress from the quasi-static stress-strain curve, b is a constant, and $\dot{\varepsilon}_p$ is the plastic strain rate. [8]

Shock Waves.

If the impact velocity is much greater than the material sound speed for a uniaxial strain state, elastic waves will be overcome as discussed earlier. This leads to the formation of shock waves, which are narrow regions in which state properties vary discontinuously. This discontinuity causes the conservation equations to break down when they are in differential form.

The shock wave equations developed here are for states of uniaxial strain. The equations are found by applying the conservation equations to the wave. Take a shockwave, traveling from left to right into a semi-infinite material that is stationary, stress free, and has no internal energy, see Figure 15. The two states identified by subscripts 1 and 0 represent the physical state ahead of and behind the shock respectively. The shock velocity is U, while the local particle velocity is u.

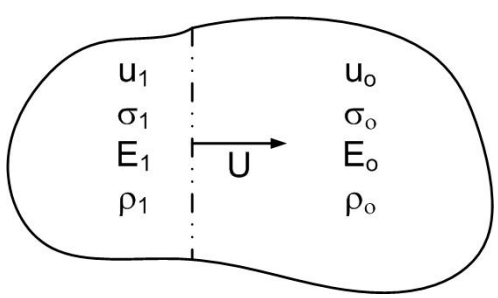

Figure 15 – Conditions at a Shock Front [7]

First, the conservation of mass across the shock states that the mass flow entering the shock must equal the mass flow leaving the shock. The particle velocity in front of the shock, u_o, is zero, stationary. Mathematically, the conservation of mass is

$$\rho_o dA(u_o - U)\Delta t + \rho_1 dA(U - u_1)\Delta t = 0 \qquad (20)$$

where the mass entering the shock from the right is $\rho_o dA(u_o\text{-}U)\Delta t$, and from the left is $\rho_1 dA(U\text{-}u_1)\Delta t$. Eliminating the dA and Δt, we obtain,

$$\rho_o U = \rho_1 (U - u_1)\,. \qquad (21)$$

Second, the conservation of momentum is developed. The change in momentum across the shock must equal the impulse applied, or

$$\rho_o dAU\Delta t u_1 = \sigma_1 dA\Delta t\,. \qquad (22)$$

This can be simplified to give the shock wave physics definition of stress,

$$\sigma_1 = \rho_o U u_1\,. \qquad (23)$$

Lastly, conservation of energy says that initial internal energy plus any work done on the system is equal to the final internal energy,

$$IE_0 + W_{0\to 1} = IE_1 \qquad (24)$$

where IE_0 is the initial internal energy, IE_1 is the final internal energy, and $W_{0\to 1}$ is the work done on the system from state zero to one. The internal energy is the sum of the internal energy source per unit mass, E, plus the kinetic energy of the mass, KE,

$$IE_0 = E_0 + KE_0 \text{ and } IE_1 = E_1 + KE_1\,. \qquad (25)$$

The internal energy source per unit mass can be a chemical reaction that releases energy, or a material with some strain energy that is stored, or other forms. Initially the kinetic energy is zero, because u_o is zero. In the final state the kinetic energy is,

$$KE_1 = \frac{1}{2}(\rho_o U \Delta t)(u_1)^2 \tag{26}$$

where $\rho_o U \Delta t$ is the mass of material which is moving, and u_1 is the velocity at which it is moving. After the shock has passed, the internal energy source is

$$\left(\rho_1 (U - u_1)\Delta t\right) E_1 \tag{27}$$

where the mass is found using the velocity relative to the shock. The combination of Equations 26 and 27 yield the internal energy after the shock has passed as,

$$IE_1 = \frac{1}{2}(\rho_o U \Delta t)(u_1)^2 + \left(\rho_1 (U - u_1)\Delta t\right) E_1 \tag{28}$$

The internal energy source in front of the shock is,

$$IE_0 = \left(\rho_o U \Delta t\right) E_o \tag{29}$$

where the term in the parentheses is the mass of material with the internal energy E_o. Because the mass in front of the shock was assumed stationary, this also happens to be the internal energy of the mass.

As for the work done on the system, work is known to be a force carried out over some distance, which is,

$$W_{0\to 1} = \sigma_1 (u_1 \Delta t)\,. \tag{30}$$

If Equations 28, 29, and 30 are combined, the conservation of energy equation for a moving shock wave is

$$\left(\rho_o U\Delta t\right)E_o + \sigma_1 u_1 \Delta t = \left(\rho_1 (U - u_1)\Delta t\right)E_1 + \frac{1}{2}(\rho_o U\Delta t)(u_1)^2 . \qquad (31)$$

Eliminating Δt and rearranging so that the internal energy terms are on the same side,

$$\left(\rho_1 (U - u_1)\right)E_1 - \rho_o U E_o = \sigma_1 u_1 - \frac{1}{2}(\rho_o U)(u_1)^2 . \qquad (32)$$

The second term on the left hand side can be simplified using conservation of mass, and the second term on the right hand side can be simplified using conservation of momentum, giving

$$\left(\rho_1 (U - u_1)\right)E_1 - \rho_1 (U - u_1)E_o = \sigma_1 u_1 - \frac{1}{2}\sigma_1 u_1 . \qquad (33)$$

The right side can be simplified and dividing through by $\rho_1 (U - u_1)$ which gives

$$E_1 - E_o = \frac{1/2\ \sigma_1 u_1}{\rho_1 (U - u_1)} . \qquad (34)$$

Then, solving the conservation of momentum equation for u_1 and substituting into the above equation gives

$$E_1 - E_o = \frac{\frac{1}{2}\sigma_1 \left(\frac{U(\rho_1 - \rho_o)}{\rho_1}\right)}{\rho_1 \left(U - \frac{U(\rho_1 - \rho_o)}{\rho_1}\right)} . \qquad (35)$$

U can be eliminated, and finding a common denominator on the bottom gives

$$E_1 - E_o = \frac{\frac{1}{2}\sigma_1 \left(\rho_1 - \rho_o\right)}{\rho_1 \rho_o} . \qquad (36)$$

Finally, simplifying one step further gives the commonly used conservation of energy equation for shock waves,

$$E_1 - E_o = \frac{1}{2}\sigma_1\left(\frac{1}{\rho_o} - \frac{1}{\rho_1}\right). \tag{37}$$

This is called the Hugoniot relation. [9]

The conservation equations by themselves present an incomplete picture of shock waves. The three equations (Equations 21, 23, and 37), which are referred to as the Hugoniot equations, contain five unknowns, U, u, E, σ, and ρ. One of the two remaining independent variables is found through the use of a Hugoniot curve, which is the locus of all attainable shock states that are possible in a material. The other independent variable is found from measurement or knowledge of one variable from the equation of state, discussed in a subsequent section. A Hugoniot curve is analogous to a stress-strain curve in uniaxial stress, but it is not developed from one experiment that follows the loading path leading to equilibrium from a uniaxial stress state. Instead, the curve is developed using many planar impact experiments, such as Flyer Plate experiments [10], to describe the relationship between hydrostatic pressure and specific volume, see Figure 16.

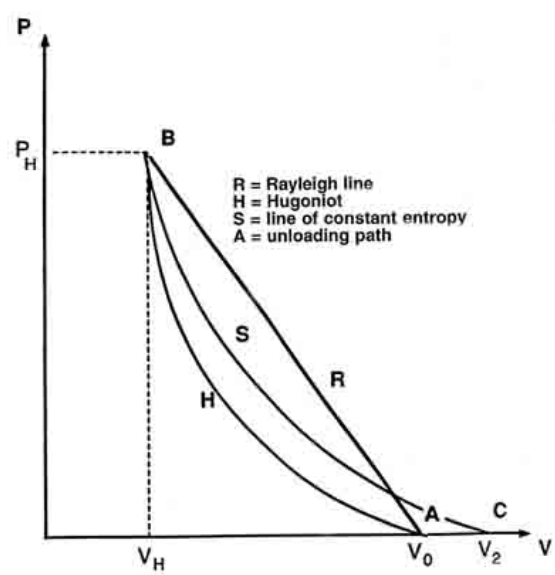

Figure 16 – Hugoniot Curve Showing Loading and Unloading Paths [7]

Each point in a Hugoniot curve represents a separate experiment, and hence, each point is an equilibrium state for a specific experiment. [9] In this figure, the Hugoniot curve is marked as H. When an impact occurs the loading path follows the line from point A where the material has zero pressure but high velocity, to point B along what is called the Rayleigh line. The loading does not follow the Hugoniot, but rather occurs along a straight line connecting the initial state with the peak pressure of impact, P_H, which is on the Hugoniot curve. Unloading occurs isentropically along the line marked S, which is not along the Hugoniot curve. [9]

Hugoniot curves are only valid in certain situations because they are developed under uniaxial strain shock wave conditions. However, another use of Hugoniot data is that it assists in the development of equations of state, which are more general. [7] Computer codes that solve impact problems use an equation of state to relate internal energy, pressure, and volume. Like a Hugoniot, an equation of state is developed using planar impact experiments.

Constitutive Equation

A constitutive equation is the relationship between stress and strain used by continuum mechanics codes. As stated before, the stress-strain relation in most metals produces two distinct areas of response to a loading, quasi-static and dynamic. In most finite element codes, stress is assumed to be quasi-static, which means that the loading is applied so slowly that there aren't any dynamic loading effects. Hooke's Law is a common quasi-static model used to understand the stress-strain curve,

$$\sigma = f(\varepsilon, E_m) \tag{38}$$

where σ is the stress, ε is the strain, and E_m is the modulus of elasticity. However, Hooke's Law will only be used in cases where the stress is below the yield stress of the material. In cases where the applied stress is greater than the yield stress, it is necessary to account for dynamic loading effects. The most common way to account for dynamics is to include strain rate as a variable in the constitutive equation. In general this becomes,

$$\sigma = f\left(\varepsilon, \dot{\varepsilon}, E_m\right) \tag{39}$$

where $\dot{\varepsilon}$ is the strain rate applied. In some cases, constitutive equations will also be a function of internal energy and damage. [11] In dynamic problems under large pressure, heating due to plasticity must be accounted for. Therefore, temperature is required in a constitutive equation.

Constitutive equations exist for metals, ceramics, concrete, soil, and others. There are also numerous constitutive equations with which stress-strain behavior can be modeled. Only one of which will be used in this study, the Johnson-Cook equation.

The Johnson-Cook Strength Model presents the von Mises flow stress as

$$\sigma = (A + B\varepsilon^n)\left(1 + C\ln\dot{\varepsilon}_p(1 - T^{*m})\right) \tag{40}$$

where σ is the von Mises flow stress, ε is the equivalent plastic strain, $\dot{\varepsilon}_p$ is the plastic strain rate normalized by a strain rate of $1.0s^{-1}$, *A, B, C, m,* and *n* are known as the Johnson-Cook coefficients. The model accounts for temperature via the homologous temperature T^* as

$$T^* = \frac{T - T_{room}}{T_{melt} - T_{room}} \tag{41}$$

where T is the absolute temperature, T_{room} is the ambient temperature, and T_{melt}, is the melting temperature of the material. [7]

There is one minor disadvantage to the Johnson-Cook model. The model presents strain rate sensitivity as being independent of temperature, which generally is not the case. The upside to this is that by keeping strain, strain rate, and temperature uncoupled, it is relatively straightforward to determine the coefficients from a few experiments at various temperatures and strain rates. This fact will be utilized in the subsequent sections.

Equation of State

The equation of state (EOS) describes the behavior of hydrostatic components of stress and strain. It can be thought of as a three-dimensional constitutive equation which expresses the possible states a material can achieve. Equations of state are needed to model how pressure, density, and energy relate when compressibility effects and irreversible processes such as shock waves are included in the problem. In fact, when the pressure is very high, the EOS takes over for the constitutive equation. Energy needs to be considered in the analysis because shock wave conditions result from high strain rate deformation. [12]

Stress and strain can be broken down into two components, the hydrostatic or volumetric stress or strain and the deviatoric stress or strain,

$$[\sigma] = [\sigma_h] + [\sigma_d] \tag{42}$$

where [σ] is the stress tensor, [σ_h] is the hydrostatic stress tensor, and [σ_d] is the deviatoric stress tensor. The hydrostatic stress, or volumetric stress, is associated with volume changes, whereas, deviatoric stress is associated with shape change. The two are handled by separate relationships in impact problems. The deviatoric stress relationships were discussed in the constitutive equation section. The hydrostatic stress relationship is the EOS.

The equation of state can be shown in a general form of

$$E = E(P,V) \tag{43}$$

where E is the internal energy, P is the pressure, and V is the specific volume. An alternative form, often used in computer codes is,

$$P = P(\rho, E)\,. \tag{44}$$

There are many different forms of equations of states that are commonly used in solving impact problems, one of which will be discussed here. The Mie-Grüneisen form is simple and good for modeling high-pressure shock related events. [10] It is based upon statistical mechanics, using the energy of individual atoms to arrive at thermodynamic equations. As stated earlier, the Hugoniot is one of the pieces of information used to develop equations of state. Here, the Hugoniot pressure is used as a baseline in the Mie-Grüneisen EOS and is given by a third order polynomial,

$$P_H = C_1\mu + C_2\mu^2 + C_3\mu^3 \tag{45}$$

where P_H is the Hugoniot pressure, the C_i*'s* are constants, and μ is defined as

$$\mu = \frac{\rho}{\rho_o} - 1. \tag{46}$$

The C parameters are only for cases where density increases. If density decreases, C_2 and C_3 are zero. The pressure is then calculated as

$$P = P_H\left(1 - \frac{\Gamma\mu}{2}\right) + \Gamma\rho\left(E - E_o\right) \tag{47}$$

where E is the internal energy per unit mass, E_o is the internal energy per unit mass at ambient conditions, and Γ is a constant called the Grüneisen parameter. This parameter is assumed only as a function of specific volume, and is represented as

$$\Gamma = V\left(\frac{\partial P}{\partial E}\right)_v . \tag{48}$$

In this investigation, CTH will be used to analytically model gouging. CTH doesn't use an equation for the EOS. Instead, it uses a table of pressure, energy, and density at various states, called the SESAME model. There are two advantages for using a table, first, there is no need to calculate equation of state variables, and second, the exact physical state is used as opposed to an assumed state, i.e. a quadratic form as in the Mie-Grüneisen equation.

Buckingham Pi Theorem

Dimensional analysis will allow an investigation of the local Rod Impact Model, both experimentally and analytically (CTH), to be applied to the sled-slipper-rail system at the HHSTT. The Buckingham Pi Theorem is one such tool for dimensional analysis, and will be used to develop a set of variants that can scale a model so that numerical results and experimental results can be applied and conclusions drawn about the actual physical structure.

According to the Buckingham Pi Theorem, if a physical law consists of a number of quantities, $\{q_i\}^m$, that have dimension and are products and powers of *j* independent fundamental dimensions, L_j, then a unit free fundamental law can be defined as

$$f\left(q_1, q_2, q_3, \cdots, q_m\right) = 0 \tag{49}$$

where *m* is the number of dimensioned quantities to be used in the analysis [13]. A fundamental dimension is a quantity that is used to describe a dimensioned quantity. There are many different fundamental systems that can be used such as FLT (Force, Length, Time) and MLT (Mass, Length, Time). Take pressure for example, in the FLT system, pressure would be represented as FL^{-2}, in the MLT system, pressure is represented as $ML^{-1}T^{-2}$. It must be ensured that the fundamental dimensions alone can describe all dimensioned quantities.

As mentioned above, it is possible to represent any dimensioned quantity as a product of fundamental dimensions raised to some power

$$q_i = \left[L_1^{\,d_1} L_2^{\,d_2} \cdots L_n^{\,d_n} \right]_i \tag{50}$$

where q_i is a dimensioned quantity, L_j is a fundamental dimension, and d_k is the power the fundamental dimension is raised to. The dimensioned quantities can then be combined to form invariant Pi quantities

$$\Pi = \left(q_1\right)^{\alpha_1} \left(q_2\right)^{\alpha_2} \cdots \left(q_m\right)^{\alpha_m} \tag{51}$$

where the α_i*'s* are a to be determined exponent. It then follows that

$$\Pi = \left(L_1^{\,d_1} L_2^{\,d_2} \cdots L_n^{\,d_n}\right)^{\alpha_1}{}_1 \left(L_1^{\,d_1} L_2^{\,d_2} \cdots L_n^{\,d_n}\right)^{\alpha_2}{}_2 \cdots \left(L_1^{\,d_1} L_2^{\,d_2} \cdots L_n^{\,d_n}\right)^{\alpha_m}{}_m . \tag{52}$$

Rearranging this equation so that all of the L_i quantities are together leads to

$$\Pi = (L_1)^{\beta_1}(L_2)^{\beta_2}\cdots(L_n)^{\beta_n} \tag{53}$$

where the exponents β can be described as

$$\begin{Bmatrix} \beta_1 \\ \beta_2 \\ \vdots \\ \beta_n \end{Bmatrix} = \begin{bmatrix} d_{11} & d_{12} & \cdots & d_{1m} \\ d_{21} & d_{22} & & d_{2m} \\ \vdots & & \ddots & \vdots \\ d_{n1} & d_{n2} & \dots & d_{nm} \end{bmatrix} \begin{Bmatrix} \alpha_1 \\ \alpha_2 \\ \vdots \\ \alpha_m \end{Bmatrix}. \tag{54}$$

Mathematically, $\{\alpha\}$ must exist in the null space of the dimension matrix, *[D]* for the physical law to be dimensionally consistent. This requires that $\{\beta\} = \{0\}$. This requirement forces the solution of Equation 54 to give the products of dimensioned quantities that must remain invariant between models. [13]

Also according to the theorem, if there are m dimensioned quantities and r fundamental dimensions, then there are $k = m - r$ independent dimensionless quantities. In the MLT system there will be $r = 3$ fundamental dimensions. [13]

III. Methodology

Cinnamon [14] concurrently developed a one-dimensional approach for predicting penetration depth that is used to predict gouging at the HHSTT. He verified his work with a series of four oblique ballistic impact experiments. This work will compare computer simulations of these experiments to the measured depths. This is done so as to yield multiple studies from the same experiment. Then, through the Buckingham Pi Theorem, this model is scaled up to an equivalent HHSTT sled system. While this equivalent system might not physically exist, it will give ballpark estimates of what similar systems should experience under the same conditions.

Cinnamon Experiments

The Cinnamon experiments consist of a cylindrical projectile with a hemispherical tip impacting a target at an oblique angle. The projectiles are fired from a 30 mm powder gun as shown in Figure 17 with velocities on the order of 2.2 km/s.

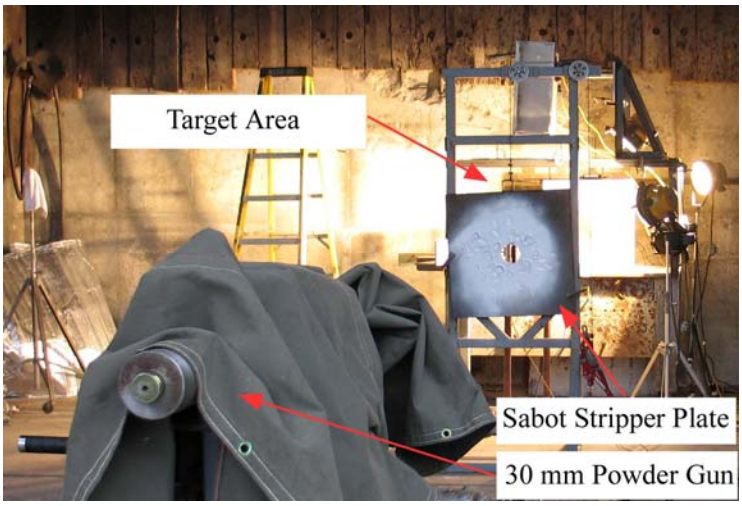

Figure 17 – 30 mm Powder Gun

The projectiles are placed in a plastic sabot designed to separate midair, which impact the sabot stripper plate. The projectiles pass through the hole in the center of the stripper plate, enter the target area, and impact the target, see Figure 18. A steel "pusher plate" is placed at the base of the projectile to prevent the projectile from lodging into the sabot during launch. Two high speed cameras digitally capture the event at 47,000 frames per second.

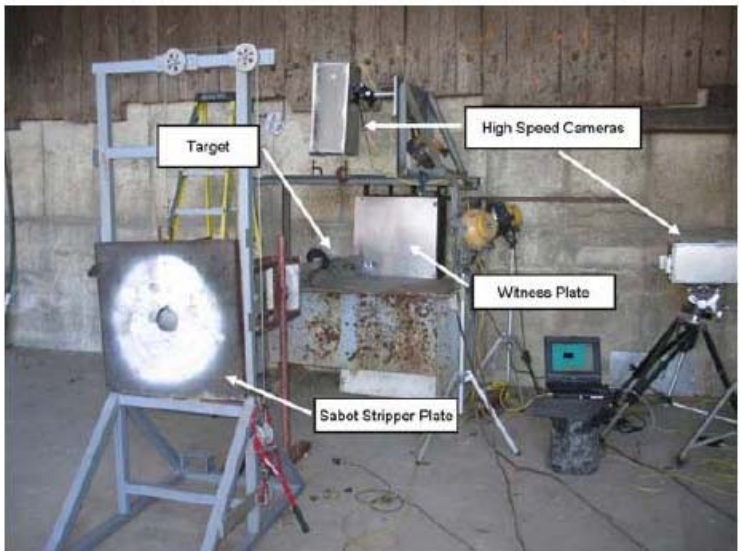

Figure 18 – Experimental Target Area

Holloman AFB supplied the projectiles and targets, which are an 18 inch section of rail from the HHSTT. Figure 19 shows a close-up of the target rail. The expected direction of travel and impact zone of the projectile is also shown. The target orientation was changed to match the desired impact angle.

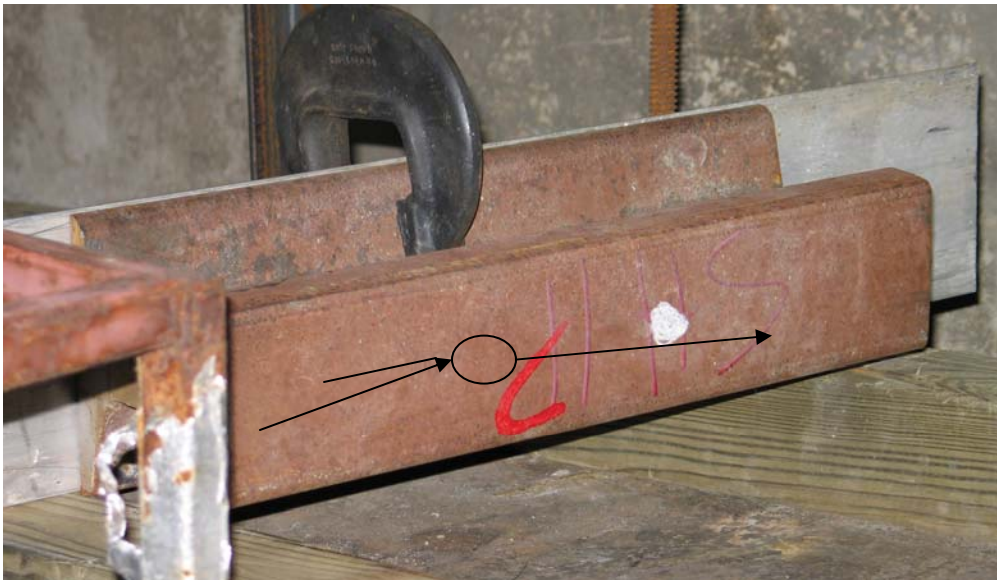

Figure 19 – Experimental Target

It is worthy to mention that the projectiles fired during the experiment did not have desired flight stability as in normal firearms. Ordinary firearms have a spiral grove

machined down the bore of the barrel. The projectile, whose diameter matches the diameter of the barrel, will spin axially as it travels down and exits the barrel. This spinning stabilizes the projectile during flight. The gun barrel used in this analysis has no grove and is designed around the sabot. Multiple sabot configurations allows multiple projectile sizes to use be fired from the same gun. Hence, the sabot and projectile did not spin and have a natural instability during flight.

Four tests were performed by Cinnamon. Figure 20 through Figure 21 show the gouge for tests 1 and 2. Direction of travel is left to right in all photographs.

Figure 20 – Experimental Test 1 Gouge

Figure 21 – Experimental Test 2 Gouge

Tests #3 and #4 were fired at a different target rail of the same material. Figure 22 through Figure 24 show before and after photos of the target rail for tests 3 and 4.

Figure 22 –Target Rail for Tests 3 and 4, Before Test

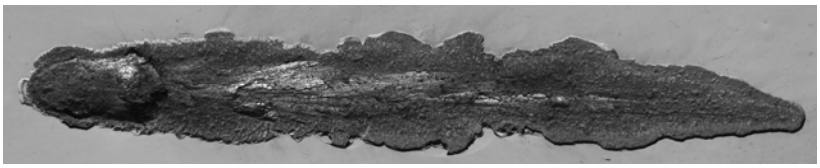

Figure 23 – Experimental Test 3 Gouge

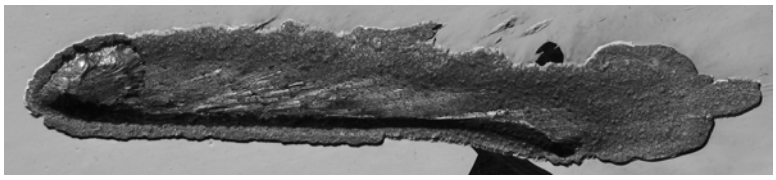

Figure 24 – Experimental Test 4 Gouge

As mentioned earlier, it is assumed that the projectile is not aerodynamically stable, which leads to tumbling. Figure 21 shows indirect evidence of this. Scuff marks are seen on the upper side of the gouge area, suggesting that the projectile impacted at an angle relative to the axial centerline. However, the high speed cameras did reveal that the projectile had a flat orientation relative to the target.

It is also worth mentioning here that the two target rails have different surface preparations. Target rail #1 is uncoated, while target rail #2 has an epoxy coating. The effect of coatings on gouging is not within the scope of this work.

Table 1 lists the velocities, impact angles, velocity components, and measured depths of the experiments. The measurements were made by taking a clay mold of the gouges. It was attempted to "soft catch" the projectiles after impact for analysis. However, the projectiles disintegrated upon impact and were not recoverable.

Table 1 – Cinnamon Experiment Results

Parameter	Test 1	Test 2	Test 3	Test 4
v (m/s)	2225	2150	2147	2163
Angle (deg)	10	15	15	10
u_x (m/s)	2191.20	2076.74	2073.84	2130.14
u_y (m/s)	-386.37	-556.46	-555.68	-375.60
Measured Depth (mm, ± 0.1 mm)	0.5	1.0	1.0	0.5

Model Development

In his work for the HHSTT, Szmerekovsky utilized the Buckingham Pi theorem to scale his model so that he represented the actual physical problem, but on a smaller scale. The Szmerekovsky Model is a simplified plane-strain model of the HHSTT sled system. It consists of a typical sled system and modeled as being evenly distributed across four shoes. The flow chart showing how he simplified the system is seen in Figure 25.

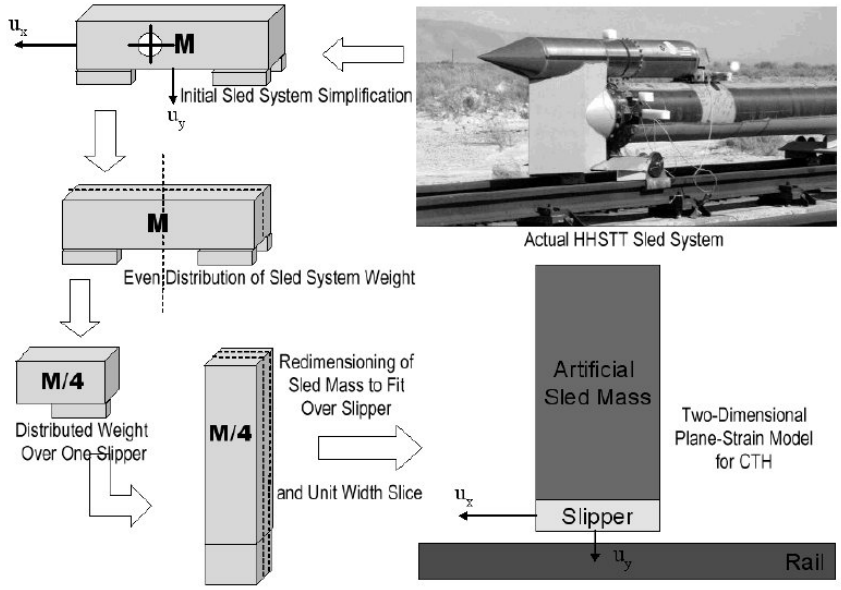

Figure 25 – HHSTT Sled Simplification

Here it is seen that the model assumes ¼ the total mass on one slipper and taking a unit width slice to end up with the 2D plane strain model.

Szmerekovsky used the conservation equations as the physical laws to be applied to the Buckingham Pi Theorem, as will this work. Table 2 lists the variables that Szmerekovsky used.

Table 2 – Buckingham Pi Input Variables

	Component	Symbol
Geometry	Length	l
	Width	w
	Height	d
Velocity	Horizontal	u_x
	Vertical	u_y
Material Properties	Density	ρ
	Sound Speed	c
	Compressive Yield	$\sigma_{y,c}$
	Elastic Modulus	E_o
	Shear Modulus	G_o
Energy	Kinetic Energy	E
	Internal Source Energy	S
Mass	Mass	m

The selection of variables is one of the most critical steps in applying the Buckingham Pi Theorem. The more variables included, extraneous or not, the higher the chances are that some of the resulting parameters will be costly or nearly impossible to match between models. Most engineering problems involve certain simplifying assumptions that influence the selection of variables. A suitable balance between simplicity and accuracy is the desired goal. How accurate the solution is depends on the objective of the study. Rickerd performed a Buckingham Pi analysis that resulted in nine invariants, two of which proved impossible to match. This analysis will use the following reasoning to reduce the number of input variables, in order to further refine the important parameters in hypervelocity gouging. If a particular variable is a function of other variables that are included in the analysis, then it can be removed with no decrease in accuracy. This is because the Buckingham Pi Theorem will ensure proper scaling of the component variables, and hence, the removed variable is forced to be scaled indirectly. [13] Table 3 lists the changes to the input variables for the analysis.

Table 3 – Buckingham Pi Variable Selection Changes

Change	Variable	Reason
Remove	w	Plane Strain analysis
Remove	S	S = 0 for model
Remove	E	E = f(m, u_x, u_y)
Remove	c	c = f(E_m, ρ), ρ = f(m, l, h)
Remove	ρ	ρ = f(m, l, h)
Add	t	Include time scale

The changes to the Buckingham Pi input variables results nine variables which gives a total of six invariants that must be matched between models. The invariant parameter Π is then

$$\Pi = (m)^{\alpha_1} (l)^{\alpha_2} (d)^{\alpha_3} (u_x)^{\alpha_4} (u_y)^{\alpha_5} (\sigma_{y,c})^{\alpha_6} (E_m)^{\alpha_7} (G_o)^{\alpha_8} (t)^{\alpha_9} . \qquad (55)$$

Table 4 lists the dimensions of the Π parameter in terms of the fundamental dimensions M, L, and T.

Table 4 – Buckingham Pi Dimensioned Quantities

Dimensioned Quantity	**Symbol**	**Fundamental Dimensions**
Mass	m	M
Height	d	L
Length	l	L
Horizontal Velocity	u_x	LT^{-1}
Vertical Velocity	u_y	LT^{-1}
Compressive Yield Strength	$\sigma_{y,c}$	$ML^{-1}T^{-2}$
Elastic Modulus	E_o	$ML^{-1}T^{-2}$
Shear Modulus	G_o	$ML^{-1}T^{-2}$
Time	t	T

In fundamental dimension form, Equation 52 becomes

$$\Pi = (M)^{\alpha_1}(L)^{\alpha_2}(L)^{\alpha_3}\left(LT^{-1}\right)^{\alpha_4}\left(LT^{-1}\right)^{\alpha_5}\left(ML^{-1}T^{-2}\right)^{\alpha_6}\left(ML^{-1}T^{-2}\right)^{\alpha_7}\left(ML^{-1}T^{-2}\right)^{\alpha_8}(T)^{\alpha_9}. \quad (56)$$

This reduces to

$$\begin{aligned}
&\Pi = (M)^{\beta_1}(L)^{\beta_2}(T)^{\beta_3} \\
&\text{where,} \\
&\beta_1 = \alpha_1 + \alpha_6 + \alpha_7 + \alpha_8, \\
&\beta_2 = \alpha_2 + \alpha_3 + \alpha_4 + \alpha_5 - \alpha_6 - \alpha_7 - \alpha_8, \\
&\beta_3 = -\alpha_4 - \alpha_5 - 2\alpha_6 - 2\alpha_7 - 2\alpha_8 + \alpha_9.
\end{aligned} \quad (57)$$

Setting the values of β to zero and solving for $m = \alpha_1$, $l = \alpha_2$, and $u_x = \alpha_4$ gives

$$\begin{aligned}
&\alpha_1 = -\alpha_6 - \alpha_7 - \alpha_8, \\
&\alpha_2 = -\alpha_3 + 3\alpha_6 + 3\alpha_7 + 3\alpha_8 - \alpha_9, \\
&\alpha_4 = -\alpha_5 - 2\alpha_6 - 2\alpha_7 - 2\alpha_8 + \alpha_9.
\end{aligned} \quad (58)$$

Rewriting these equations in vector form gives

$$\begin{Bmatrix} \alpha_1 \\ \alpha_2 \\ \alpha_3 \\ \alpha_4 \\ \alpha_5 \\ \alpha_6 \\ \alpha_7 \\ \alpha_8 \\ \alpha_9 \end{Bmatrix} = \begin{Bmatrix} 0 \\ -1 \\ 1 \\ 0 \\ 0 \\ 0 \\ 0 \\ 0 \\ 0 \end{Bmatrix} C_3 + \begin{Bmatrix} 0 \\ 0 \\ 0 \\ -1 \\ 1 \\ 0 \\ 0 \\ 0 \\ 0 \end{Bmatrix} C_5 + \begin{Bmatrix} -1 \\ 3 \\ 0 \\ -2 \\ 0 \\ 1 \\ 0 \\ 0 \\ 0 \end{Bmatrix} C_6 + \begin{Bmatrix} -1 \\ 3 \\ 0 \\ -2 \\ 0 \\ 0 \\ 1 \\ 0 \\ 0 \end{Bmatrix} C_7 + \begin{Bmatrix} -1 \\ 3 \\ 0 \\ -2 \\ 0 \\ 0 \\ 0 \\ 1 \\ 0 \end{Bmatrix} C_8 + \begin{Bmatrix} 0 \\ -1 \\ 0 \\ 1 \\ 0 \\ 0 \\ 0 \\ 0 \\ 1 \end{Bmatrix} C_9. \tag{59}$$

The columns of Equation 59 represent a separate invariant. The invariant is found by associating each dimensioned quantity with its corresponding α value and raising the dimensioned quantity to the power seen in the column vector. In this case, the invariants are given by

$$\Pi = \left(\frac{d}{l}\right)^{C_3} \left(\frac{u_y}{u_x}\right)^{C_5} \left(\frac{\sigma_{y,c} l^3}{m u_x^{\,2}}\right)^{C_6} \left(\frac{E_o l^3}{m u_x^{\,2}}\right)^{C_7} \left(\frac{G_o l^3}{m u_x^{\,2}}\right)^{C_8} \left(\frac{t u_x}{l}\right)^{C_9} \tag{60}$$

The separate invariants are found by setting one $C = 1$ and the others to zero, which gives

$$\begin{aligned} \pi_1 &= \frac{d}{l} \\ \pi_2 &= \frac{u_y}{u_x} \\ \pi_3 &= \frac{\sigma_{y,c} l^3}{m u_x^{\,2}} \\ \pi_4 &= \frac{E_o l^3}{m u_x^{\,2}} \\ \pi_5 &= \frac{G_o l^3}{m u_x^{\,2}} \\ \pi_6 &= \frac{t u_x}{l} \end{aligned} . \tag{61}$$

To maintain proper scaling, these six parameters must be matched in both the Rod Impact Model and the HHSTT model. π_1 of Equation 61 defines the geometry aspect ratio, π_2 defines the impact angle. π_3 through π_5 of Equation 61 relate material properties, length, mass, and horizontal velocity. π_6 is a time scale that can be used to compare the two models.

Rod Impact Model.

The Rod Impact Model will now be developed, which is based on data from the Cinnamon experiments. The Szmerekovsky simplified HHSTT sled model, CTH simulation model, and the Buckingham Pi results are based on a plane-strain analysis. Theoretically, a plane-strain rectangular rod must be used in the experiment for the comparison to be accurate. One key problem, however, is that most high velocity impact experiments are performed using cylindrical projectiles, which are axisymmetric. As a solution, experimental results are based on cylindrical projectiles with a hemispherical end, axisymmetric, while the CTH results will be based on a plane-strain rectangular rod with a cylindrical end. The impacting end of the rod will have a curved tip because a right circular cylinder would introduce too great of a discontinuity when the 90° corner of the cylinder struck the impact plate. Analytically, CTH can perform an oblique impact analysis using only a plane-strain rectangular rod. Therefore, the CTH Rod Impact Model will be based on a plane-strain rectangular rod impacting a target at an oblique angle. Figure 26 shows the model. A subsequent section compares an axisymmetric and plane-strain model to provide a means of comparing experiment to computer simulation.

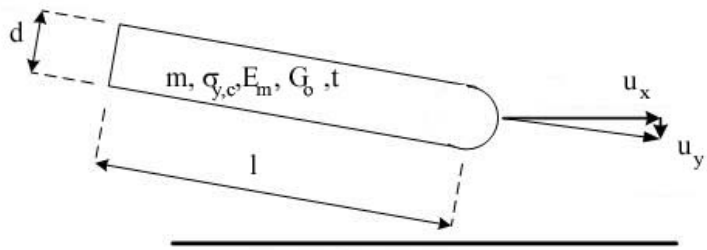

Figure 26 – Rod Impact Model

The material for the Rod Impact Model was chosen to be the same as the HHSTT, forcing the material properties to be constrained. The projectile dimensions, mass, and material properties are listed in Table 5.

Table 5 – Rod Impact Projectile Properties

m	4.78 g
l	2.5 cm
d	0.55 cm
$\sigma_{y,c}$	1.447 GPa
E_o	184.2 GPa
G_o	71.8 GPa

Using the velocity components of the Cinnamon experiments in Table 1, the Rod Impact Π invariants of Equation 61 are listed in Table 6.

Table 6 – Rod Impact Model Parameters

Parameter	**Test 1**	**Test 2**	**Test 3**	**Test 4**
v (m/s)	2225	2150	2147	2163
Angle (deg)	10	15	15	10
u_x (m/s)	2191.20	2076.74	2073.84	2130.14
u_y (m/s)	-386.37	-556.46	-555.68	-375.60
π_1	0.220	0.220	0.220	0.220
π_2	-0.1763	-0.2679	-0.2679	-0.1763
π_3	0.9851	1.0967	1.0998	1.0424
π_4	125.4061	139.6102	140.0007	132.6984
π_5	48.8825	54.4192	54.5714	51.7250

Equivalent HHSTT Sled System.

The equivalent HHSTT sled system is developed from the invariants of Equation 61. It should be noted that the invariants by themselves do not define a specifically sized equivalent system. Some information about the typical HHSTT sled system is required to enable scaling of the remaining components. For instance, the only invariants that can yield a scaled horizontal velocity are π_2, π_3, π_4, and π_5. With the material properties constrained, π_3, π_4, and π_5 govern the theoretical horizontal velocity of the sled system. With the material property removed, the invariant becomes

$$\left(\frac{l^3}{mu_x^2}\right)_{Rod\ \mathrm{Im}\,pact} = \left(\frac{L^3}{MU_x^2}\right)_{Equivalent\ HHSTT}, \tag{62}$$

which gives the horizontal velocity as

$$U_{x_{Equivalent\ HHSTT}} = \sqrt{\left(\frac{L^3}{M}\right)_{Equivalent\ HHSTT}\left(\frac{mu_x^2}{l^3}\right)_{Rod\ \mathrm{Im}\,pact}}. \tag{63}$$

Note that lowercase letters represent the rod impact model properties, while uppercase letters represent the equivalent HHSTT system. The result of Equation 63, combined with π_2 of Equation 61, will give the theoretical velocity components of the equivalent system.

It is desired to develop an equivalent HHSTT sled system that is comparable in size to an actual sled system. Therefore, L and M in Equation 63 will reflect typical sled quantities. It should be noted that M is the plane strain equivalent mass as discussed earlier in Figure 25, so a typical slipper width is needed in addition to L and M. Table 7

lists typical sled and slipper properties that are used in this work. The slipper height is found with the given slipper length and π_1 of Equation 61.

Table 7 – Typical HHSTT Sled System Quantities

Sled Mass	200 kg
Slipper Length	20.32 cm
Slipper Width	10.8 cm

While it is preferable to match a typical slipper height, the height of the equivalent system is governed by the geometry of Rod Impact model and π_1 of Equation 61.

Figure 27 shows a model comparison. Both are plane-strain models. Chapter IV contains the complete model along with the simulation.

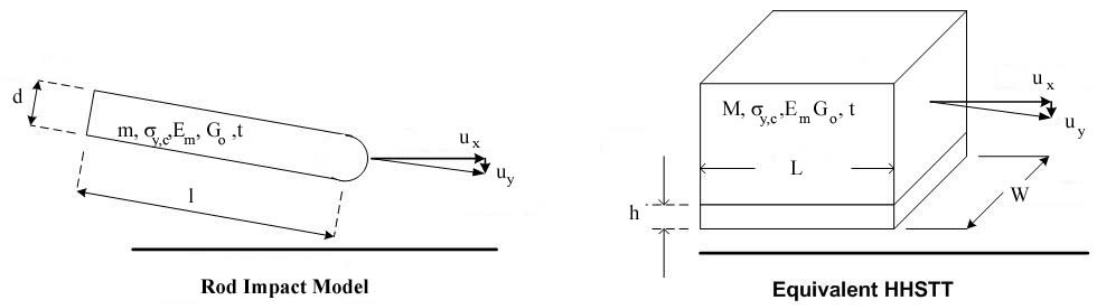

Figure 27 – Rod Impact and Equivalent HHSTT Model Comparison

As for comparing the two models in time, π_6 of Equation 61 governs the time scale between them. The time scaling is governed by

$$\left(\frac{tu_x}{l}\right)=\left(\frac{TU_x}{L}\right), \tag{64}$$

again with lowercase being the Rod Impact model and uppercase being the equivalent HHSTT sled system. This gives the equivalent HHSTT model time as

$$T = \left(\frac{L}{U_x}\right)\left(\frac{u_x}{l}\right)t\,. \tag{65}$$

CTH Model and Solution Method

Solids that undergo high strain rates and high energy impact can flow plastically in some areas, yet still maintain deviatoric stress properties. CTH is an advanced hydrocode that uses a finite volume algorithm to solve shock wave physics equations for these kinds of problems. It was developed by Sandia National Labs in the late 1980's, and was primary designed to model 3-D, multi-material, large deformation, shock wave physics [15].

Generally, there are two different ways to describe a continuum. One is a Lagrangian (material) description, in which the material is divided up into smaller pieces and the conservation equations are solved by following pieces of the material. The other is an Eulerian (spatial) description, which defines a volume in space and solves the continuity equations by tracking what goes through it.

CTH differs in the solution schemes from other mechanics codes. It employs a two-step Eulerian solution scheme. The first step starts with an Eulerian mesh which is allowed to deform in a Lagrangian manner. Conservation of volume, mass, momentum, and energy are conserved in this step. The governing equations are replaced with explicit finite volume approximations. The second step remaps the deformed shape into the original Eulerian mesh. The volume flux between cells is calculated first based on the cell face velocities. A High Resolution Interface Tracking (HRIT) algorithm is then

implemented to ensure the right materials are moved with the volume. Each material's corresponding mass, momentum, and energy is then moved.

CTH relies heavily on plots to present post-processing data. It has two basic plot types that will be used in this analysis: material and time-history plots. Material plots are one or two dimensional contour or vector plots of various properties versus position at a single timestep, as seen earlier in Figure 4. Time-history plots are plots of various properties at predefined Lagrangian tracer points versus time. These tracer point locations need to be defined in the pre-processing phase. Therefore, some knowledge of the expected regions of interest, along with trial and error is necessary for placement of these points and, ultimately, meaningful results.

CTH has numerous options and parameters at the users' disposal. Rickerd [6] investigated the proper options and parameters for modeling impacts related to the hypervelocity gouging problem and verified them experimentally. These options deal with how to handle yield strength in mixed cells, material volume fractions and pressures in mixed cells, void strength, and interface layers. Rickerd showed that allowing multiple materials and pressures in a cell, with pressure relaxation best approximates the solution.

CTH contains constitutive models that include strain and strain-rate effects that are well suited for the hypervelocity gouging problem. Standard options include rate-dependent models for material strength formulations, such as Johnson-Cook. CTH also contains two major EOS packages that are used to investigate shock-propagation, among others, which occurs in hypervelocity impacts. These are the Analytic Equation of State (ANEOS), and SNL-SESAME, a tabular EOS.

In this work, materials are modeled using the SESAME EOS package in CTH for projectile and target materials of VascoMax 300 and 1080 steel, respectively. The Johnson-Cook model for the projectile is VascoMax 300. The Johnson-Cook model for 1080 steel doesn't exist in CTH. As a solution, the target is modeled as iron with a modified yield strength to simulate 1080 steel. The works of Szmerekovsky and Rickerd have shown that this solution is adequate. Kennan [16] and Yun [17] performed a Johnson-Cook strength analysis of VascoMax 300 and 1080 steels by use of a Split Hopkinson Bar test. This data was based on strain rates on the order of up to 10^3 /s. These Johnson-Cook coefficients are used in this analysis and are listed in Table 8.

Table 8 – Johnson-Cook Coefficients

Coefficient	1080 Steel	VascoMax 300
A	525 MPa	2170 MPa
B	3.59 MPa	124 MPa
C	0.29	0.0046
m	0.7525	0.95
n	0.6677	0.3737

CTH is capable of parallel data processing, which allows simulations to run on multiple processors. All simulations in this analysis used a cluster of 64-bit Linux computers, using eight processors. On average, simulations took two hours to complete, including post-processing.

Model Boundary Conditions.

In all simulations, a semi-infinite boundary condition was used along the boundary of the mesh. When a stress wave reaches a mesh boundary, it is imagined to continue unimpeded and not reflect. Material boundaries, such as the projectile and target edges, are treated realistically, and waves reflect as dictated by theory.

CTH has three options for the treatment of material interfaces, and are summarized here:

1. No Slide Line: materials are joined at the contact surface
2. Slide Line: a frictionless sliding interface is implemented at the contact surface
3. Boundary Layer: friction is included and the sliding interface is shifted into the softer material

In a related study to the hypervelocity gouging phenomena at the HHSTT, Nguyen [18; 19] investigated the proper option, and concluded that the No Slide Line option should be implemented, and is used for all simulations.

Axisymmetric – Plane Strain Comparison.

As discussed earlier, the Cinnamon experiments used an axisymmetric cylindrical rod with a hemispherical end, whereas the CTH rod impact model is a plane-strain rectangular rod with a semicircular end. To compare the two, it is necessary to investigate how similar CTH simulates an axisymmetric and plane-strain impact of the same configuration. CTH can only simulate both in a perpendicular impact as in Figure 28. Therefore, an axisymmetric and plane-strain simulation of a vertical impact of the same length and width as the projectiles will be performed in Chapter IV. The velocity will match the y-component velocity of the actual rod impact experiments.

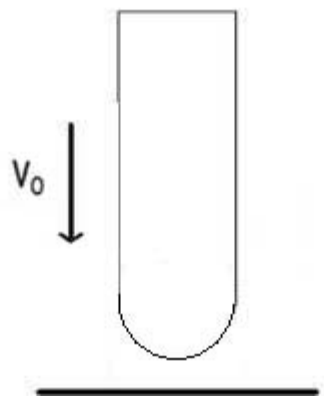

Figure 28 – Vertical Impact for Axisymmetric – Plane Strain Comparison

The mesh size in the simulation was 0.01 cm square in the region of impact of the target and throughout the rod. In the area away from the impact of the target, the mesh grows courser incrementally. A diagram of the mesh is shown in Figure 29, which is not to scale.

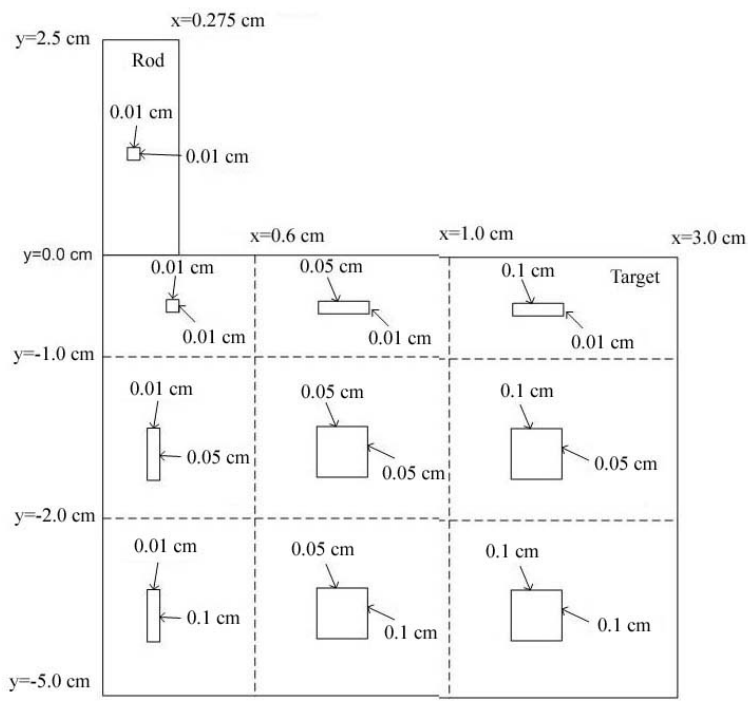

Figure 29 – Vertical Impact Mesh

For the axisymmetric simulation, only half of the model is defined. A mirror option is used during plotting to view the entire model. For the plane-strain simulation, the entire model is defined by mirroring the mesh about the left vertical edge. Appendix A contains the CTH input deck for the axisymmetric simulation.

Rod Impact Model.

For the rod impact model, the mesh was 0.005 cm square in the area of the impact. Farther from the impact zone, the mesh grows coarser incrementally. The mesh is shown schematically in Figure 30, not to scale. The rod is shaded dark gray.

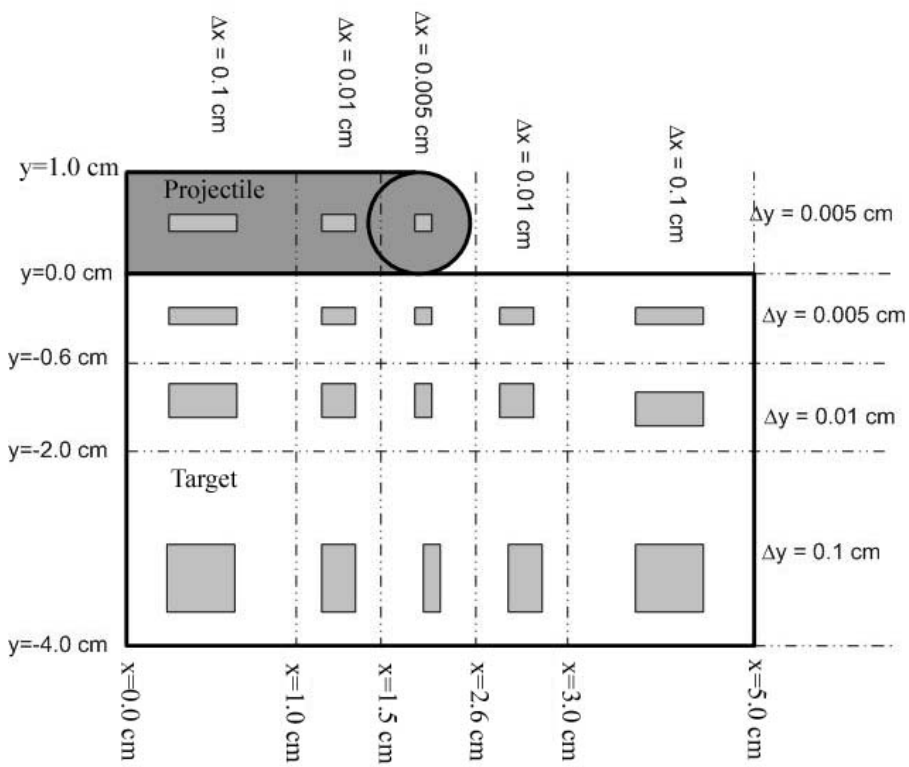

Figure 30 – Rod Impact Model Mesh

Appendix B contains the CTH input deck for the rod impact simulation #1. All other run are the same, with the exception of the velocity components.

IV. Analysis and Results

In order to simulate the Cinnamon experiments, the axisymmetric - plane-strain comparison in CTH is analyzed first. The four Cinnamon simulations follow. The results are then compared to the measured depths of the Cinnamon experiments. Using the Buckingham Pi analysis, Test #1 simulation is then scaled up to the equivalent HHSTT sled system model, which is simulated in CTH as well.

Axisymmetric – Plane-Strain Comparison

The goal of this investigation is to determine a suitable time span that a plane-strain CTH analysis can simulate an axisymmetric oblique impact. While the governing equations remain the same regardless of an axisymmetric or plane-strain analysis, the forms of the equations are different. On a local spatial scale, the differences can be dramatic, especially towards the edge of the projectile. This is due to the fact that in an axisymmetric analysis, the stress must be zero at the free end and the stress wave reflects with opposite sign, whereas, in a plane-strain analysis, the velocity is zero at the fixed end and the stress increases. However, of primary importance is how similar the simulations can predict penetration depth while maintaining similar shape, which is more on the global scale. Also of importance is how similar pressure profiles are between the two. With this said, plots of the displacement and pressure fields will be compared side-by-side. The deciding criteria for determining any dissimilarity is the time at which the displacement field within the target interior starts to differ between the two.

With the Cinnamon experimental velocities as stated above, two comparisons are investigated using vertical velocities of 375 and 550 m/s. First, the 375 m/s velocity, corresponding to Test #1 and Test #4, is analyzed. This is followed by the 555 m/s velocity analysis, corresponding to Test #2 and Test #3. Figure 31 shows the simulation at the moment of impact (*t = 0 s*) for both axisymmetric and plane-strain. It also shows the location of three Lagrangian tracer points located at (0, 0.01), (0, 0.275), and (0.275, 0.275) cm, respectively.

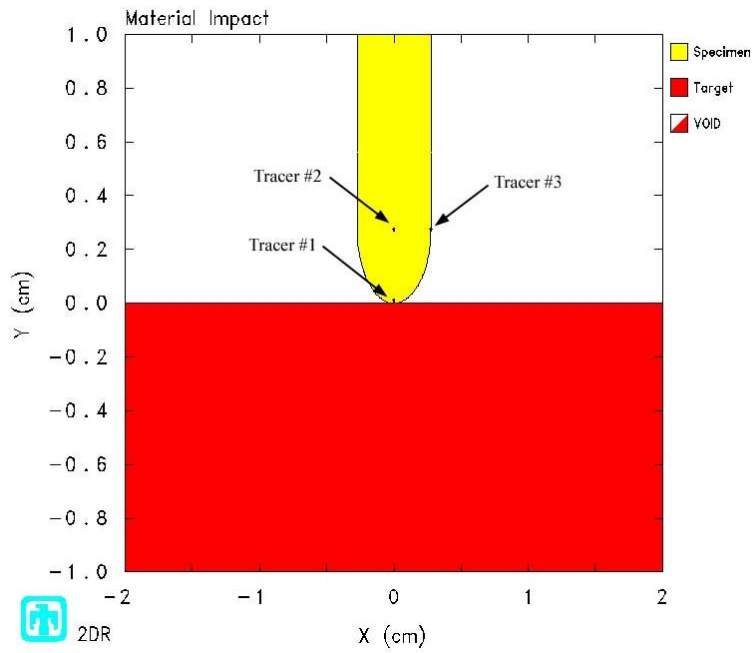

Figure 31 – Axisymmetric and Plane-Strain Comparison (t = 0 s)

375 m/s Impact Velocity.

For the 375 m/s velocity case, Figure 32 through Figure 39 show a side-by-side comparison of the displacement field of the axisymmetric and plane-strain simulations at times of 2.5, 7.5, 10.0, and 12.0 microseconds. All figures on the left are axisymmetric, and all figures on the right are plane-strain.

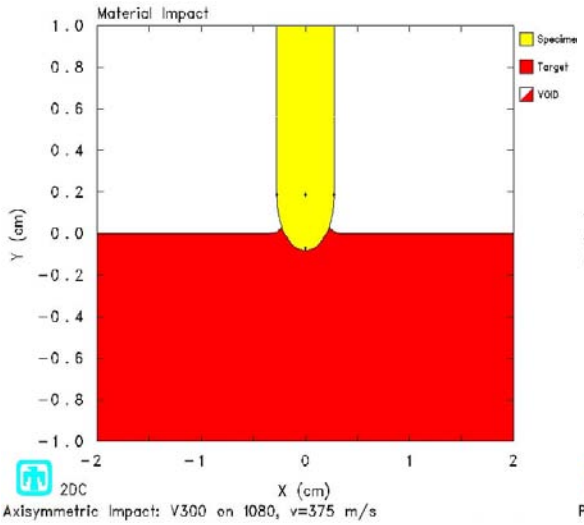

Figure 32 - v = 375, axi, t=2.5 μs

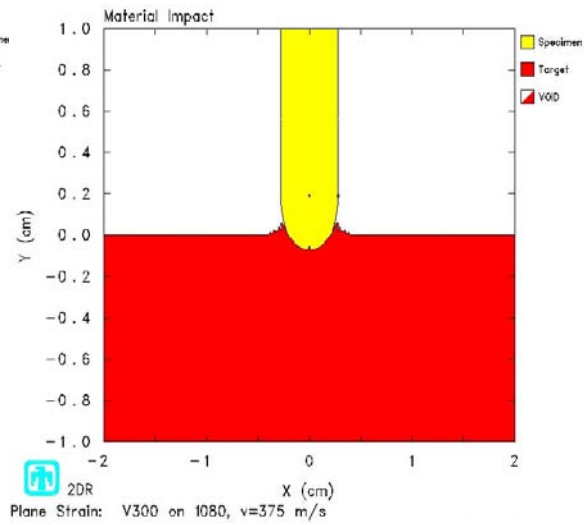

Figure 33 - v = 375, pl st, t=2.5 μs

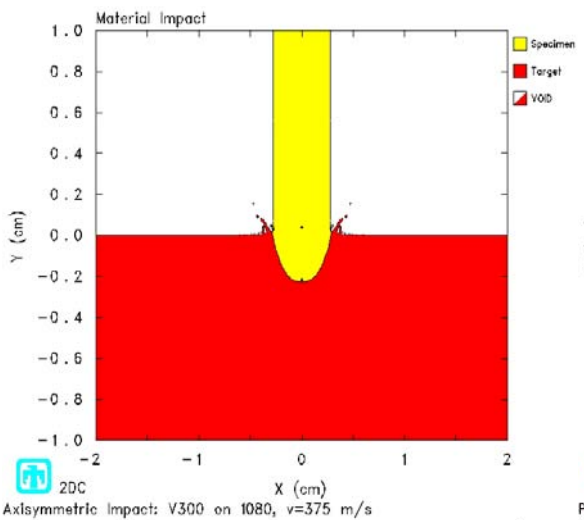

Figure 34 - v = 375, axi, t=7.5 μs

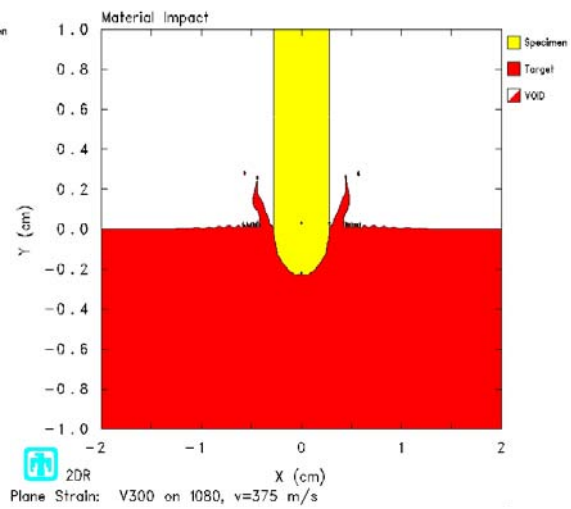

Figure 35 - v = 375, pl st, t=7.5 μs

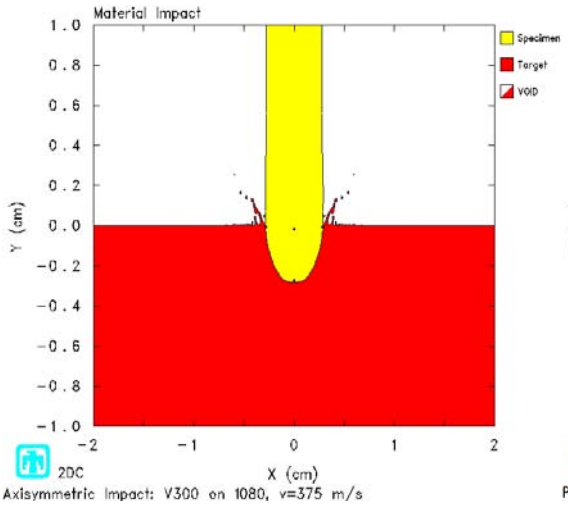

Figure 36 - v = 375, axi, t=10.0 μs

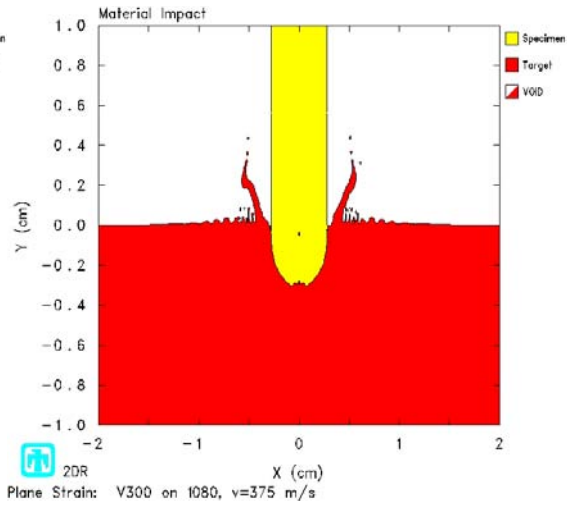

Figure 37 - v = 375, pl st, t=10.0 μs

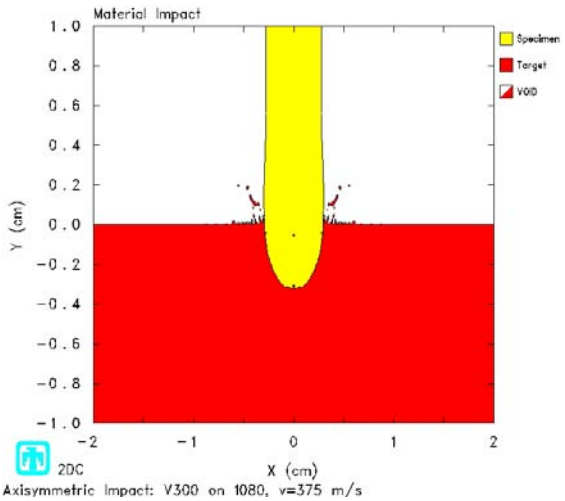

Figure 38 - v = 375, axi, t=12.0 μs

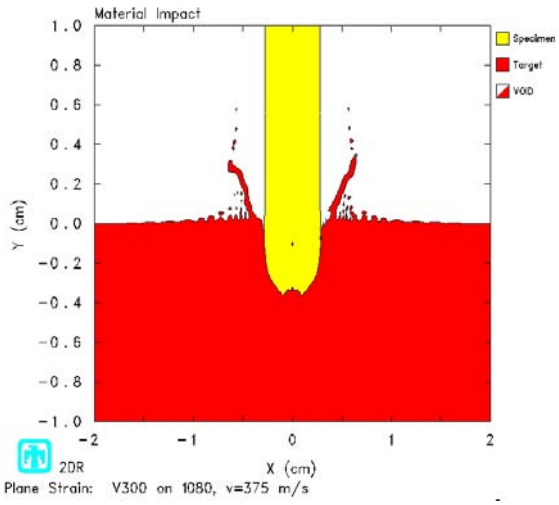

Figure 39 - v = 375, pl st, t=12.0 μs

From the very beginning, it is seen that the plane-strain analysis predicts a larger amount of target material to be displaced out and upwards of the impact zone. While this is a significant difference, the conditions at the surface of the target away from the projectile are not important. What is important is what happens in the target interior.

As the simulation progresses, a key difference is seen in the deformation of the projectile tip. At 10 μs, the projectile tip has flattened out in the axisymmetric simulation. The tip of the plane-strain simulation has already flattened and started to

form a concave down shape. At 12 μs, the flattened tip of the axisymmetric simulation has increased its flatness, while the plane-strain simulation progresses further into a concave down shape. The penetration shape of the plane-strain simulation starts to deviate from the axisymmetric version, suggesting that the projectile has started to split at the tip. This is due to the fact that the axisymmetric is 3D, whereas, the plane-strain is 1D. Because of this, 10 μs is chosen to be the maximum time limit. This implies that the plane-strain simulation of Test #1 and #4 of the Cinnamon experiments are considered accurate up to 10 μs.

The time history plots of CTH show what happens on a local spatial scale throughout the event. Figure 40 and Figure 42 show y position as a function of time of tracer points (TP) 1, axisymmetric on the left.

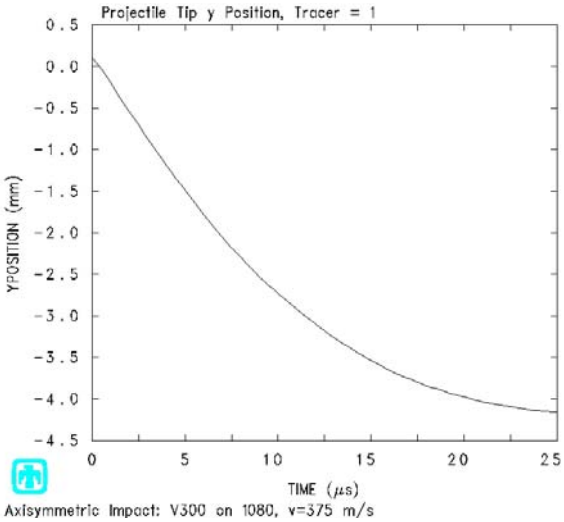

Figure 40 – TP 1 y Position, axi

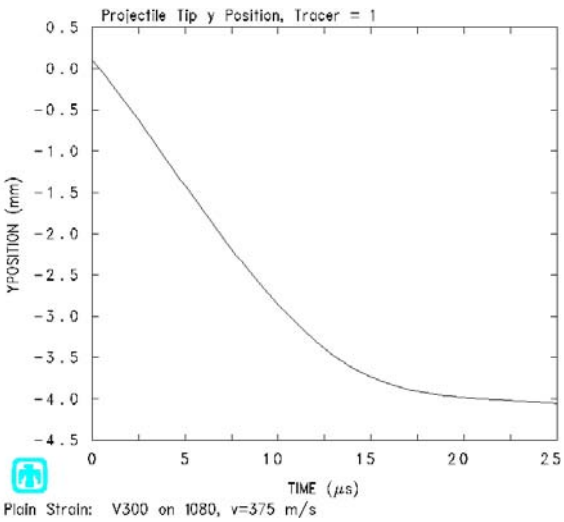

Figure 41 – TP 1 y Position, pl st

Figure 42 and Figure 44 show y position as a function of time of the projectile edge, TP 3.

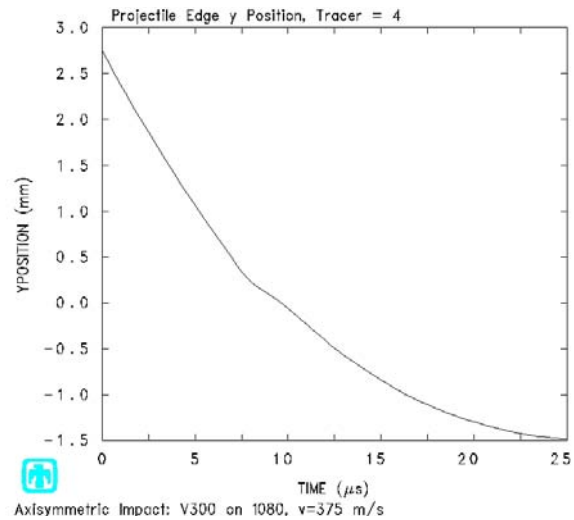

Figure 42 – TP 3 y Position, axi

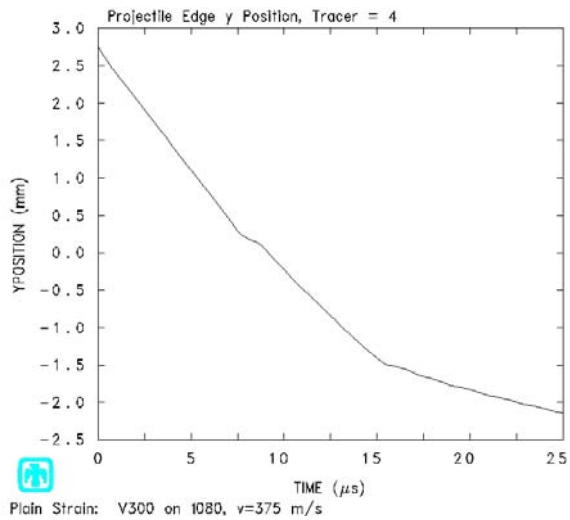

Figure 43 – TP 3 y Position, pl st

It is seen that here that the two simulations are similar up to roughly 10 μs further illustrating that the simulations are quite similar up to this point in time.

With the time span defined above, the pressure profiles are now compared. Figure 44 through Figure 49 show side-by-side comparison of pressure profiles at times of 1.5, 5.0, and 10.0 microseconds. Again, axisymmetric on the left.

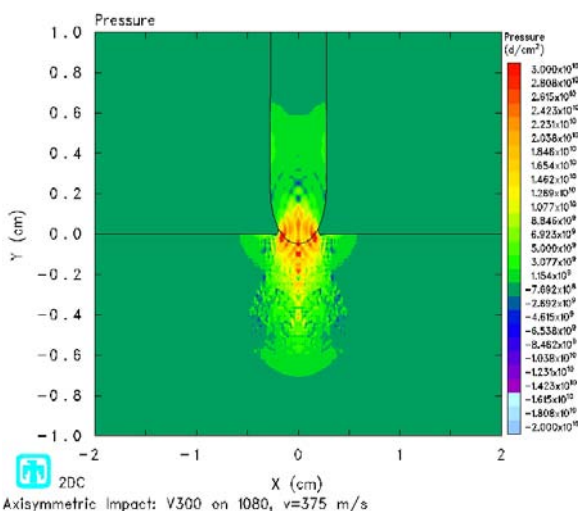

Figure 44 – Pressure, axi, t=1.5 μs

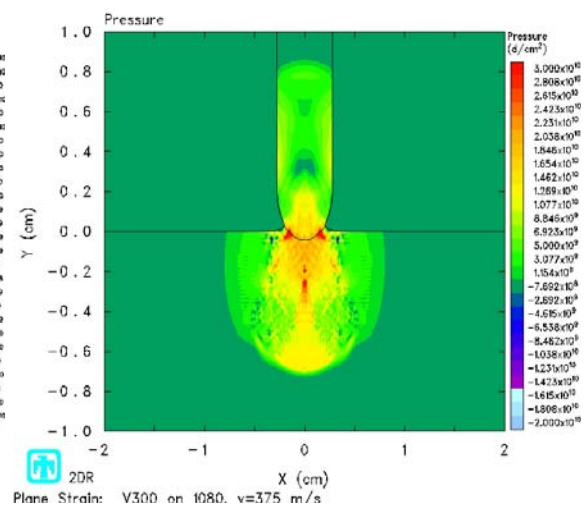

Figure 45 – Pressure, pl st, t=1.5 μs

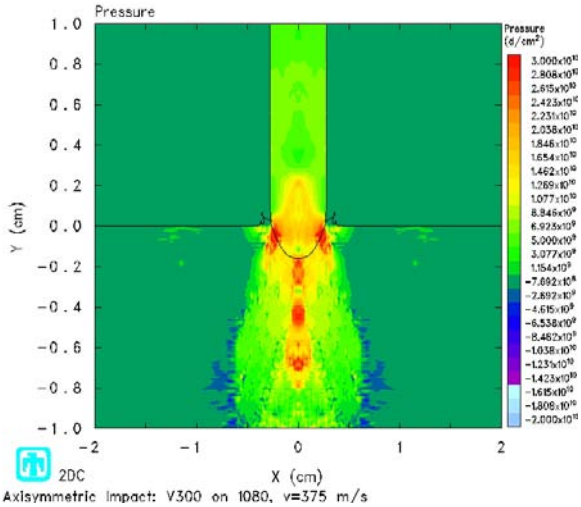

Figure 46 – Pressure, axi, t=5.0 μs

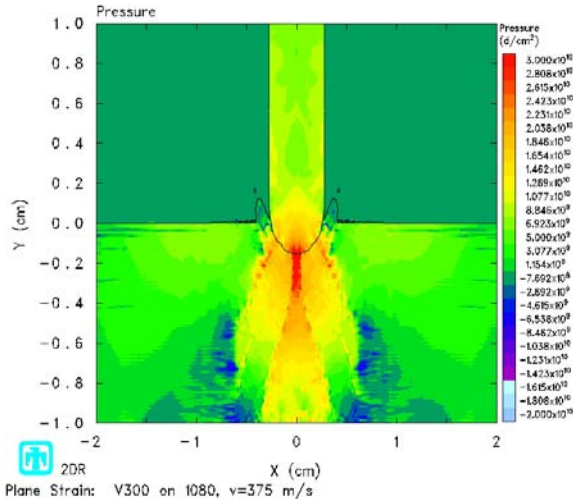

Figure 47 – Pressure, pl st, t=5.0 μs

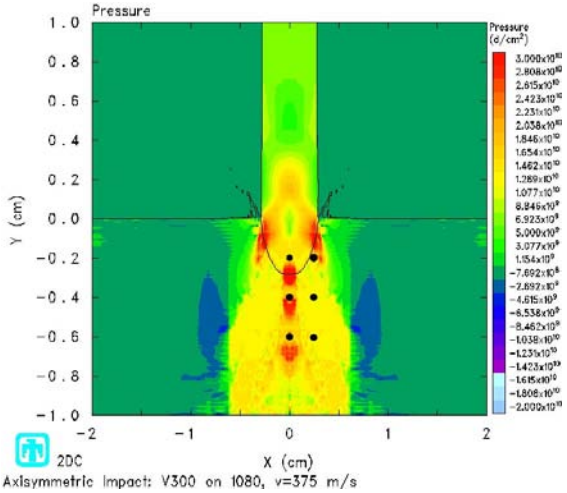

Figure 48 – Pressure, axi, t=10.0 μs

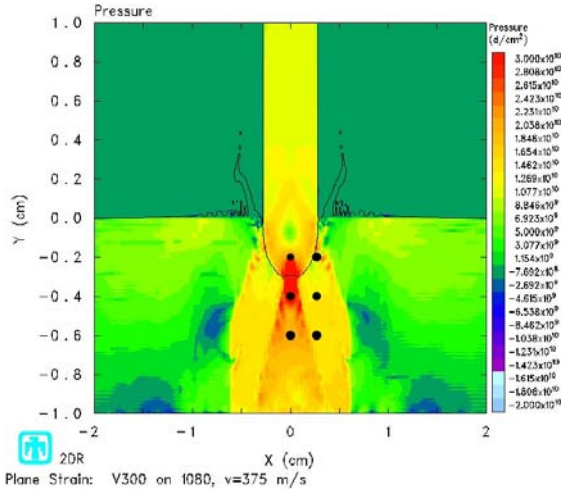

Figure 49 – Pressure, pl st, t=10.0 μs

It is seen that the two simulations differ in the profile development, but the relative difference in magnitude is not too severe. To further see the differences, Table 9 shows the relative difference of pressure at six points (in Eulerian space). Two x positions of 0 and 2.5, and three y positions of -0.2, -0.4, and -0.6 are chosen sample points, and shown on the last two figures.

Table 9 – Pressure Difference, v = 375 m/s

		Percent Difference		
x	**y**	**t=1.5 µs**	**t=5 µs**	**t=10 µs**
0	-0.2	14%	21%	16%
0	-0.4	28%	9%	14%
0	-0.6	53%	0%	16%
0.25	-0.2	52%	17%	30%
0.25	-0.4	19%	47%	0%
0.25	-0.6	19%	36%	12%
	avg	**31%**	**21%**	**14%**

This leads to the conclusion that pressure profiles in the Cinnamon simulations of Tests #1 and #4 will inherently have differences on average of 14 to 31 percent.

555 m/s Impact Velocity.

For the 555 m/s velocity, Figure 50 through Figure 57 show a side-by-side comparison of axisymmetric and plane-strain simulations at times of 2.0, 6.0, 8.0, and 10.0 microseconds. All figures on the left are axisymmetric, and all figures on the right are plane-strain.

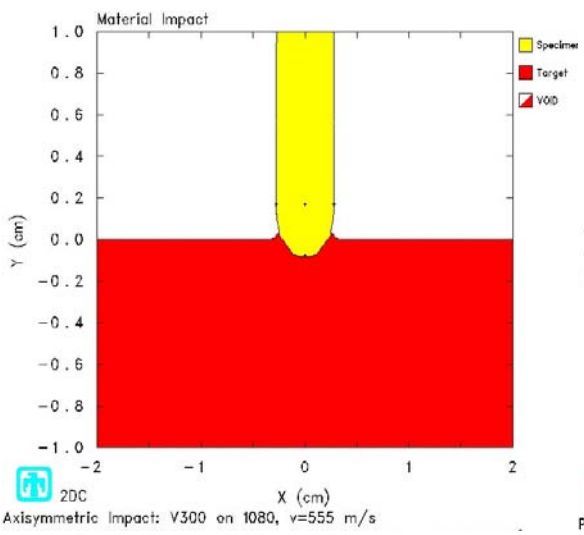

Figure 50 – v = 555, axi, t=2.0 µs

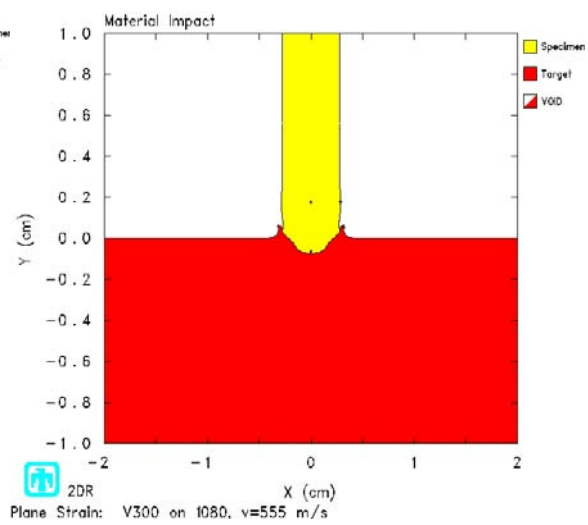

Figure 51 – v = 555, pl st, t=2.0 µs

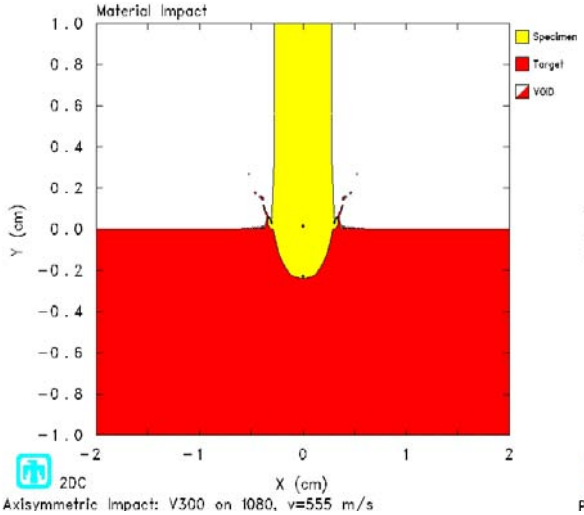

Figure 52 – v = 555, axi, t=6.0 μs

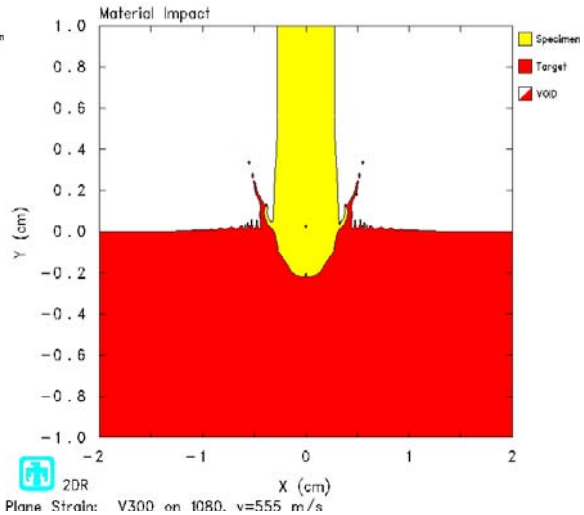

Figure 53 – v = 555, pl st, t=6.0 μs

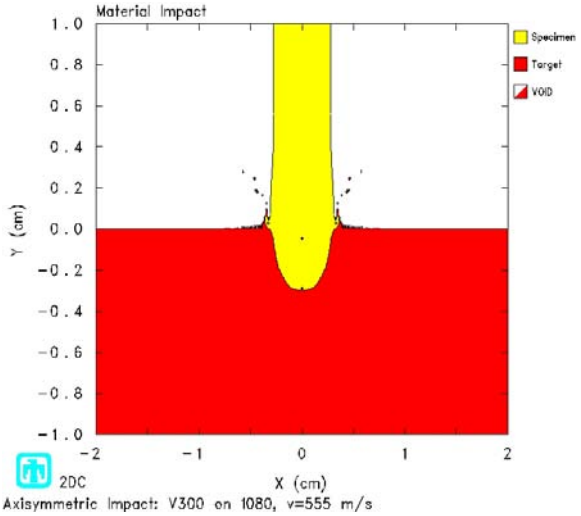

Figure 54 – v = 555, axi, t=8.0 μs

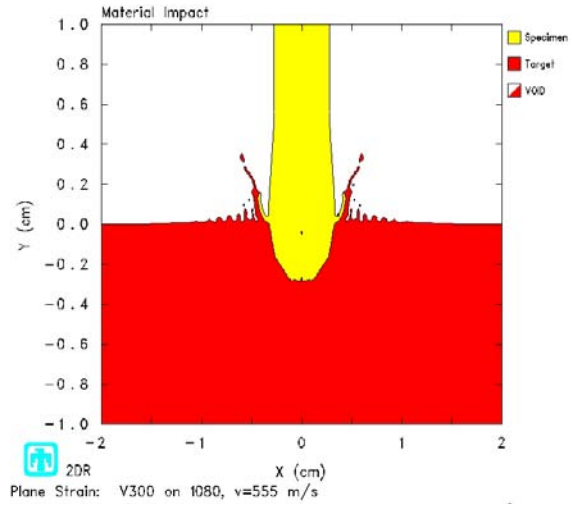

Figure 55 – v = 555, pl st, t=8.0 μs

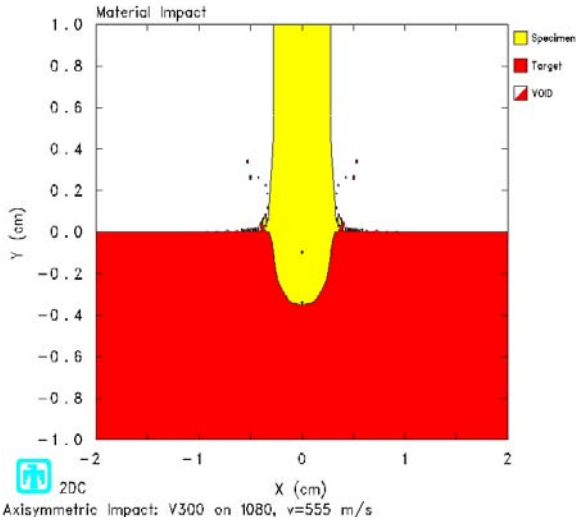

Figure 56 – v = 555, axi, t=10.0 μs

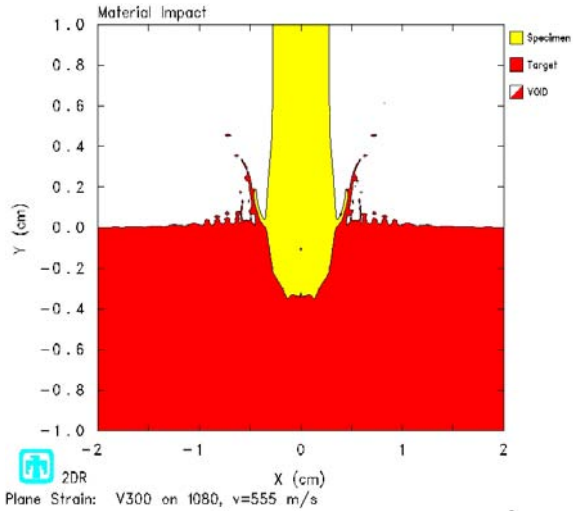

Figure 57 – v = 555, pl st, t=10.0 μs

As with the 375 m/s velocity, from the very beginning, it is seen that the plane-strain analysis predicts a larger amount of target material to be displaced out and upwards of the impact zone. Also as with the 375 m/s velocity, another difference is the manner in which the top surface of the target away from the impact deforms. The 'humps' of the plane-strain simulation are more pronounced and spread out. While these are significant differences, the conditions at the surface of the target away from the projectile are not important. What is important is what happens in the target interior.

As the simulations progress, a slight difference is seen in the deformation of the projectile along the edge, while the tip remains circular. While the plane-strain shape is not a curved as the axisymmetric, it does not worsen as time progresses. At 8 μs, the projectile tip starts to flatten out in the plane-strain simulation. At 10 μs, the axisymmetric simulation still maintains a flattened tip, while the plane-strain simulation has started to form humps at the tip. The penetration shape of the plane-strain simulation starts to deviate from the axisymmetric version. Because of this, 10 μs is chosen to be

the maximum time limit. This implies that the plane-strain simulation of Test #2 and #3 of the Cinnamon experiments are considered accurate up to 10 μs.

The time history plots of CTH show what happens on a local spatial scale throughout the event. Figure 58 and Figure 60 show the y position of tracer point 1, axisymmetric on the left.

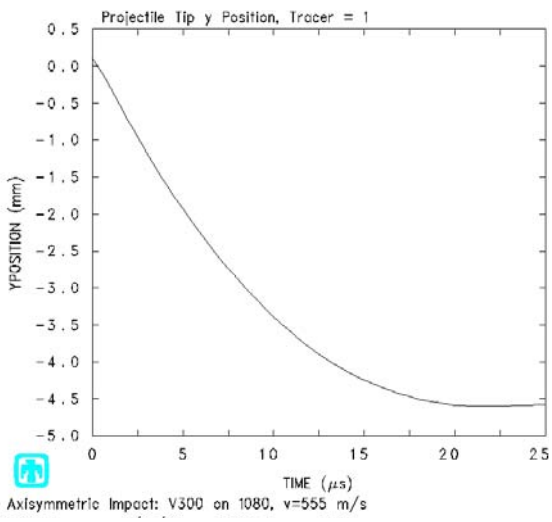

Figure 58 – TP 1 y Position, axi

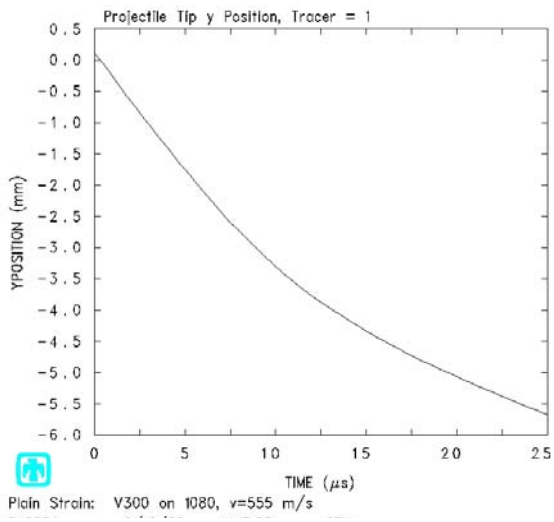

Figure 59 – TP 1 y Position, pl st

It is seen from these two figures that the two simulations are similar up to roughly 12 μs. Figure 60 and Figure 62 show the y position of the projectile edge, TP 3.

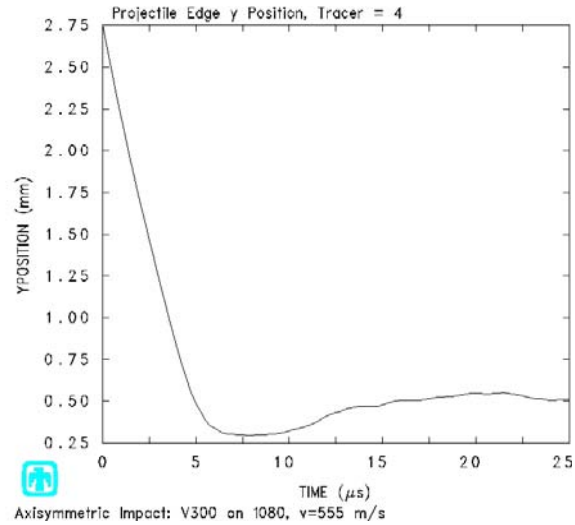

Figure 60 – TP 3 y Position, axi

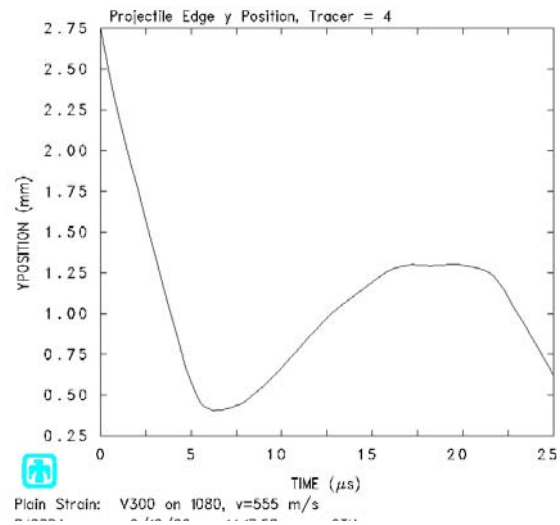

Figure 61 – TP 3 y Position, pl st

It is seen that here that the two simulations are similar up to roughly 10 μs further illustrating that the simulations are quite similar up to this point in time.

With the time span defined above, the pressure profiles are now analyzed. Figure 62 through Figure 67 show side-by-side comparison of pressure profiles at times of 1.5, 5.0, and 10.0 microseconds. Again, axisymmetric on the left.

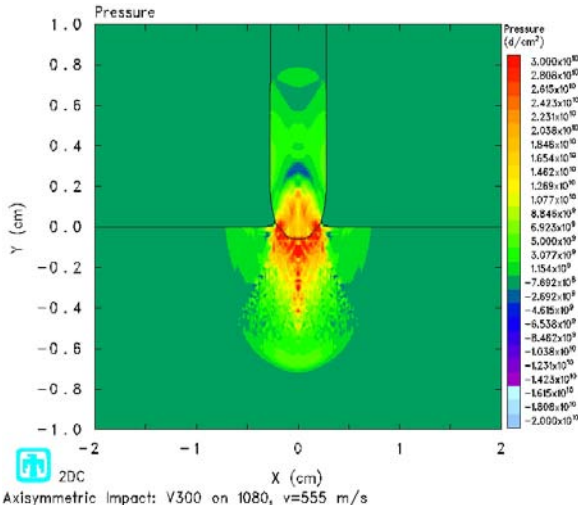

Figure 62 – Pressure, axi, t=1.5 μs

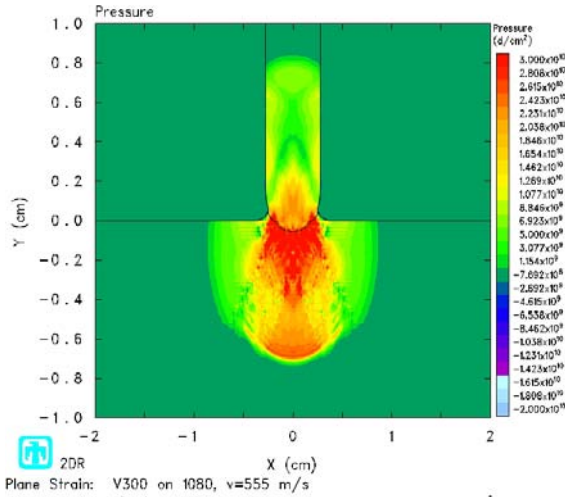

Figure 63 – Pressure, pl st, t=1.5 μs

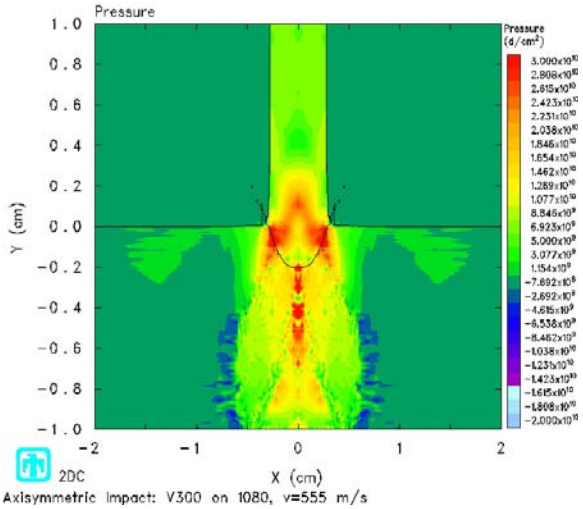

Figure 64 – Pressure, axi, t=5.0 μs

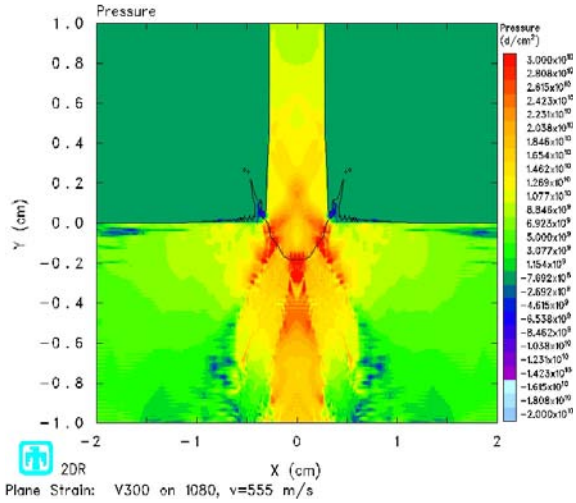

Figure 65 – Pressure, pl st, t=5.0 μs

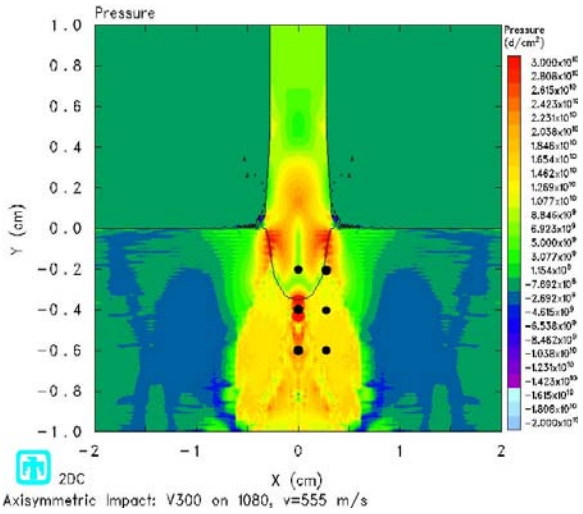

Figure 66 – Pressure, axi, t=10.0 μs

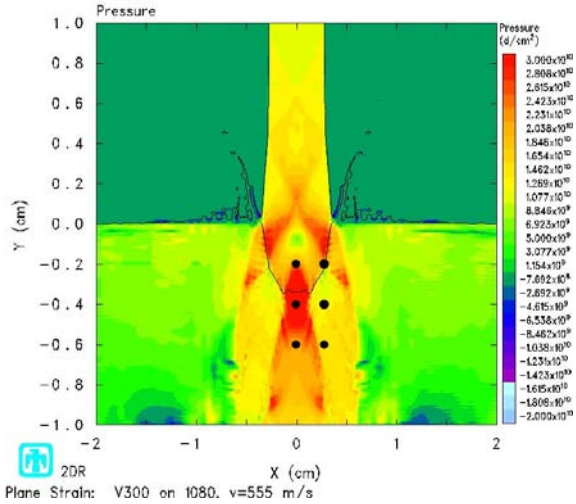

Figure 67 – Pressure, pl st, t=10.0 μs

It is seen that the two simulations differ in the profile development, but the relative difference in magnitude is not too severe. To further see the differences, Table 10 shows the relative difference of pressure at six points (in Eulerian space). Two x positions of 0 and 2.5, and three y positions of -0.2, -0.4, and -0.6 are chosen sample points, and shown on the last two figures.

Table 10 – Pressure Difference, v = 555 m/s

		Percent Difference		
x	y	t=1.5 μs	t=5 μs	t=10 μs
0	-0.2	14%	40%	74%
0	-0.4	37%	35%	0%
0	-0.6	61%	10%	0%
0.25	-0.2	16%	7%	0%
0.25	-0.4	52%	42%	13%
0.25	-0.6	52%	42%	0%
	avg	**39%**	**29%**	**14%**

This leads to the conclusion that pressure profiles in the Cinnamon simulations of Tests #2 and #3 will inherently have differences on average of 14 to 39 percent.

Bringing this all together, Table 11 shows a time range comparison between the allowed contact time of the experiment and the time limit imposed on the CTH analyses from above. The contact time was taken to be the time to transverse one full length of the projectile traveling at the horizontal velocity.

Table 11 – Time Range Comparison

Test	Velocity (m/s)	Angle (deg)	Experimental Contact Time (μs), approx.	Time of CTH Simulation (μs)	Percent Simulated
1	2225	10	11.40	10	88%
2	2150	15	12.04	10	83%
3	2147	15	12.05	10	83%
4	2163	10	11.74	10	85%

It is seen that CTH is capable of capturing most of the event, but not its entirety.

Rod Impact Simulation

With the imposed CTH time limit above, the simulations of the Cinnamon experiments are made. Figure 68 shows the configuration at the moment of impact (*t = 0 s*), for all simulations. As mentioned in the discussion of the Cinnamon experiments, the projectile is oriented level against the target with the velocity vector at the appropriate angle, as shown. The only difference between simulations is the velocity vector. The

CTH simulations of Tests #1 and #4 are analyzed first since they share the same impact angle of 10°. The analysis of Tests #2 and #3, which share the angle of 15°, follows. The simulations are stopped at 10 μs because the plane-strain simulation of the axisymmetric event is not considered accurate past this point.

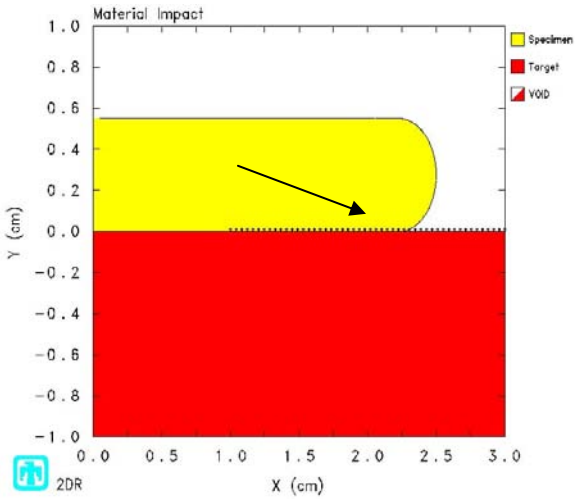

Figure 68 – CTH Rod Impact Model, (t = 0 s)

Test #1 Simulation, v=2225 m/s @ 10°.

Figure 69 through Figure 72 show the simulation at interesting times of 3.0, 4.5, 6.5, and 10.0 microseconds.

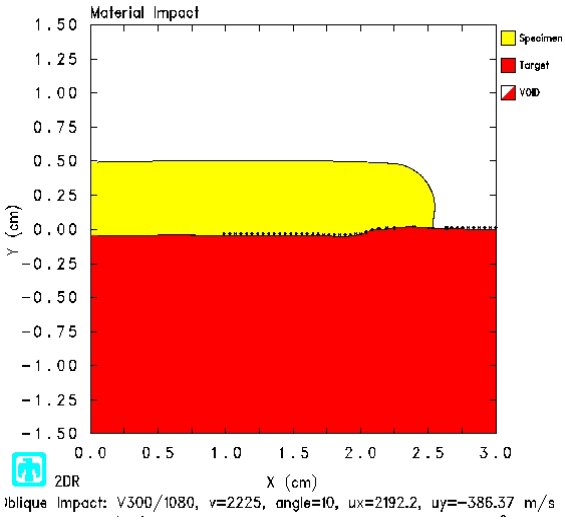

Figure 69 – Test #1 Sim, t=3.0 μs

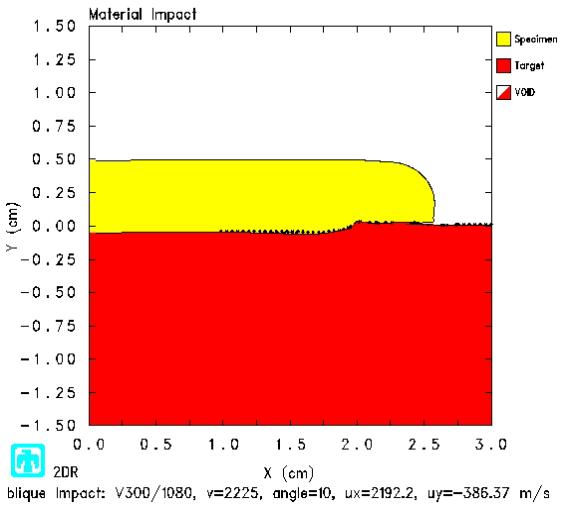

Figure 70 – Test #1 Sim, t=4.5 μs

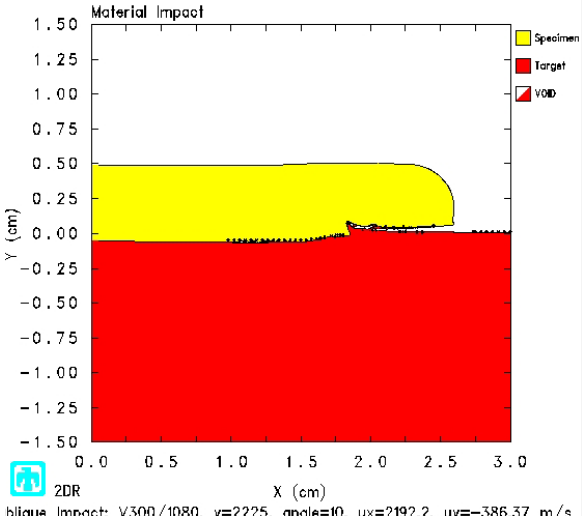

Figure 71 – Test #1 Sim, t=6.5 μs

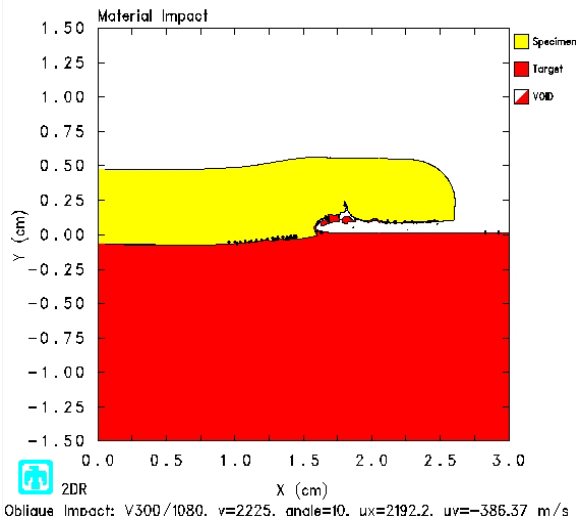

Figure 72 – Test #1 Sim, t=10.0 μs

From 3 to 4.5 μs, the projectile and target start do deform and form a gouge. At 6.5 μs, the projectile is on the verge of forming a crack. At 10 μs, the projectile crack is developing, and the penetration depth of the target is roughly 1 cm. To determine a better estimate, Figure 73 shows a blown up image of the simulation at 10 μs. Note that the x and y axis scaling are different.

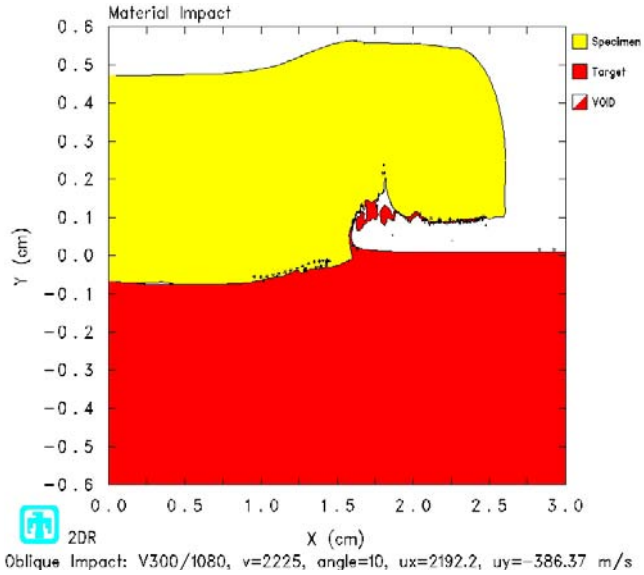

Figure 73 – Test #1 Sim, t=10 μs, zoom

It is seen that the simulated penetration depth is on the order of 0.7 cm. The measured depth is 0.5 ± 0.1 mm. The difference in depth is roughly 29 percent, which is very good.

It is also interesting to note pressure and plastic strain-rate profiles in Figure 74 and Figure 75. Due to less difference in pressure magnitudes at 10 μs, this time is chosen to better represent the pressure distribution.

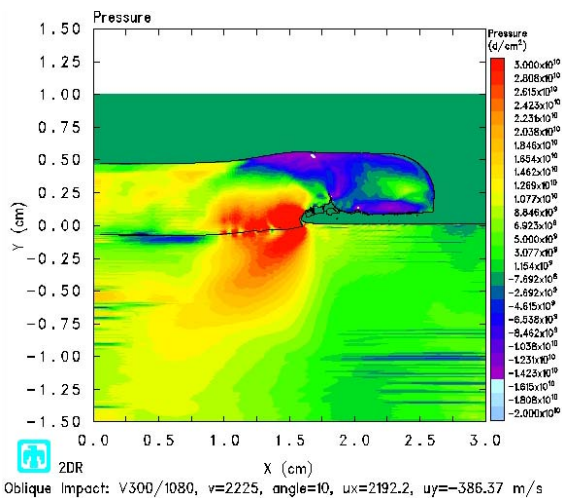

Figure 74 – Test #1 Pressure Profile, t=10.0 μs

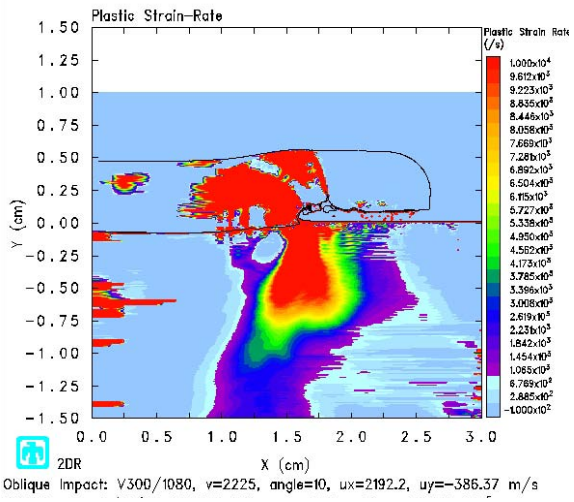

Figure 75 – Test #1 Strain Rate, t=10.0 μs

It is seen here that pressures on the order of 3.0 GPa are present, indicating that the plastic limit is exceeded and shock waves occur. It is also seen that strain-rates as high as 10^4 /s are present, indicating that although the current Johnson-Cook strength model is fairly accurate, it has just exceeded its range of applicability. As noted earlier, the Johnson-Cook strength model was based on strain rates up to 10^3 /s.

Test #4 Simulation, v=2163 m/s @ 10°.

Figure 76 through Figure 79 show the simulation at interesting times of 3.0, 4.5, 6.5, and 10.0 microseconds.

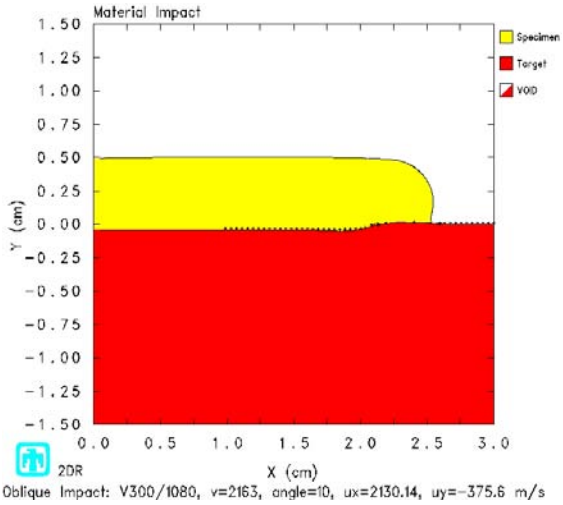

Figure 76 – Test #4 Sim, t=3.0 μs

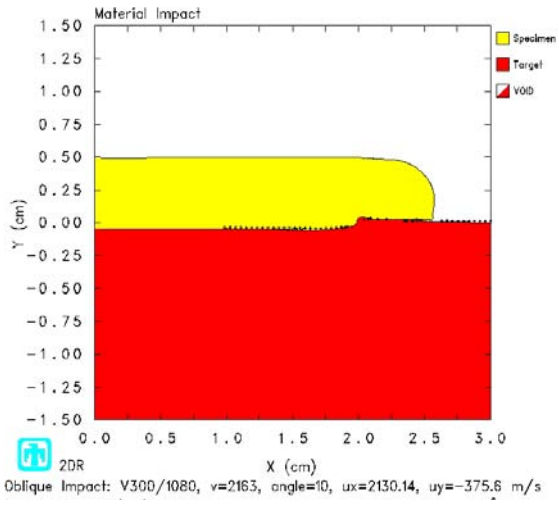

Figure 77 – Test #4 Sim, t=4.5 μs

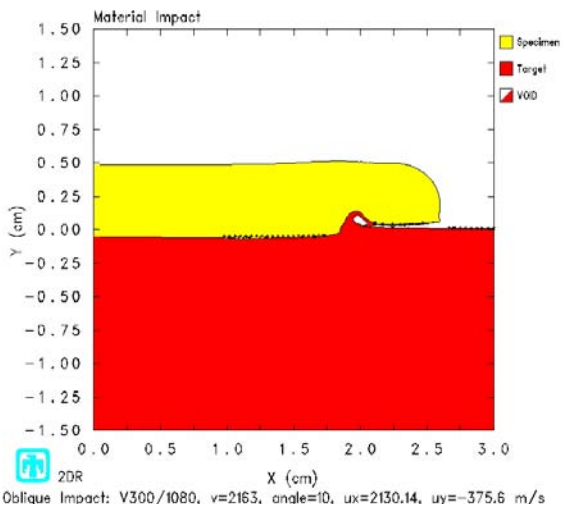

Figure 78 – Test #4 Sim, t=6.5 μs

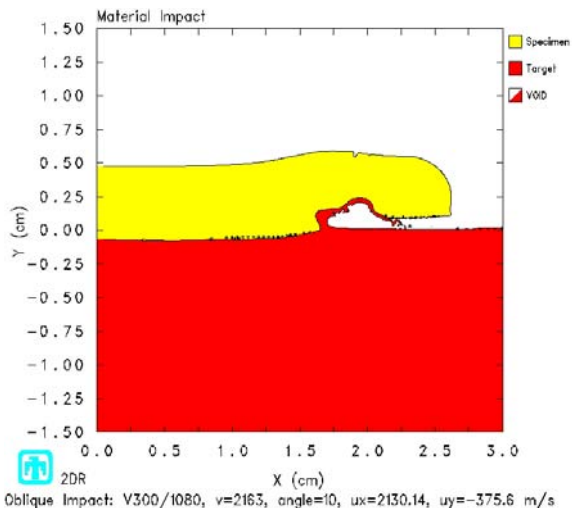

Figure 79 – Test #4 Sim, t=10.0 μs

From 3 to 4.5 μs, the projectile and target start do deform and form a gouge. At 6.5 μs, the target material has formed the classic jetting of material more typical of HHSTT gouges. At 10 μs, the projectile is developing a crack on the top side, and the penetration depth of the target is roughly 0.1 cm. To determine a better estimate, Figure 80 shows a blown up image of the simulation at 10 μs. Note that the x and y axis scaling are different.

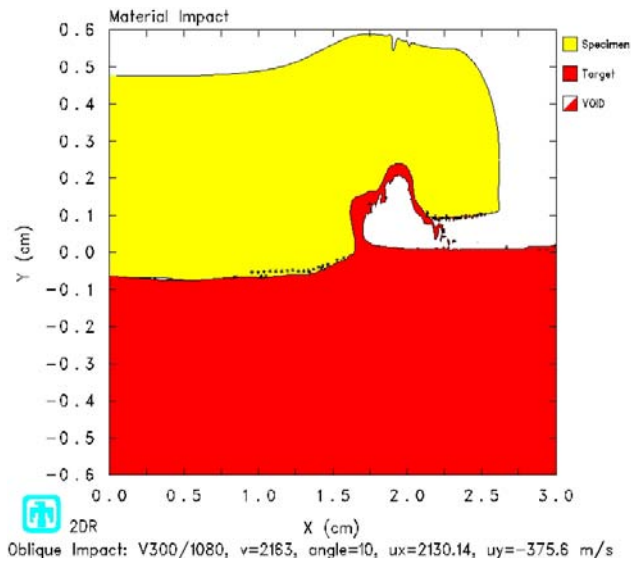

Figure 80 – Test #4 Sim, t=10.0 μs

It is seen that the simulated penetration depth is on the order of 0.7 mm. The measured depth is 0.5 ± 0.1 mm. The difference in depth is roughly 29 percent, which again is quite good. Pressure and plastic strain-rate profiles are similar to Test #1 with pressures strain rates up to 3 GPa and 10^4 /s, respectively, and are shown in Appendix C.

Compared to Test #1, a couple noticeable differences in the simulation are the target gouge formation and the projectile crack. The gouge formation in Test #4 is more pronounced than in Test #1, whereas the projectile crack is more pronounced in Test #4 than Test #1. This is due to the fact that the total velocity, and hence energy, is lower in Test #4 than Test #1.

Test #2 Simulation, v=2150 m/s @ 15°.

Figure 81 through Figure 83 show the simulation at interesting times of 2.5, 5.5, and 10.0 microseconds.

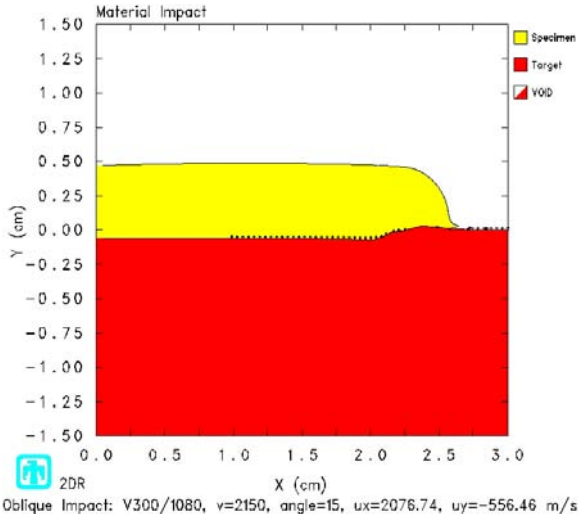

Figure 81 – Test #2 Sim, t=2.5 μs

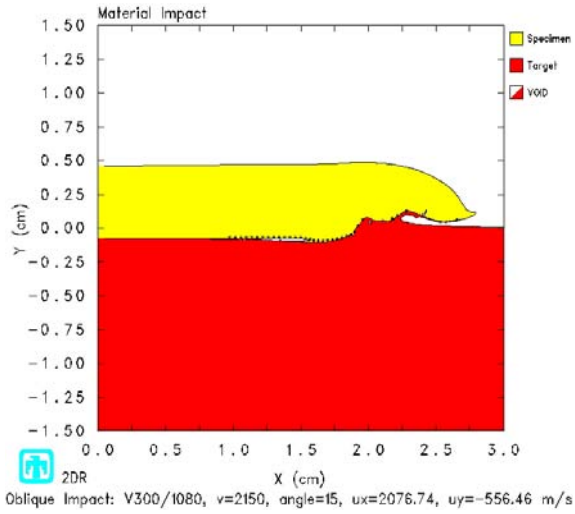

Figure 82 – Test #2 Sim, t=5.5 μs

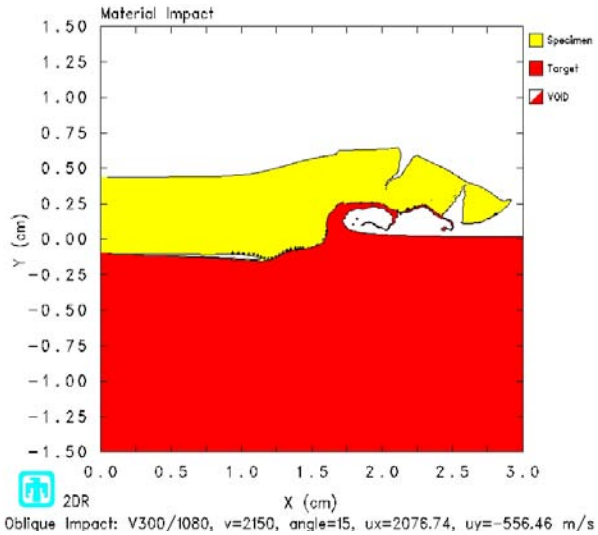

Figure 83 – Test #2 Sim, t=10.0 μs

From 2.5 to 5.5 μs, the projectile and target start do deform and form a gouge. This gouge is more pronounced than Tests #1 and #4. Also at 5.5 μs, the projectile has formed a crack on the under surface just ahead of the gouge. At 10.0 μs, the projectile has formed another crack, and both almost propagated all the way through. The penetration depth of the target is roughly 1 cm. To determine a better estimate, Figure 84 shows a

blown up image of the simulation at 10 μs. Note that the x and y axis scaling are different.

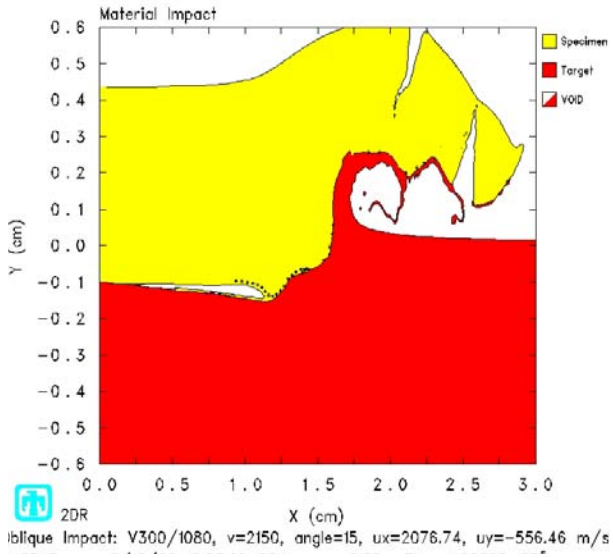

Figure 84 – Test #2 Sim, t=10.0 μs

It is seen that the simulated penetration depth is on the order of 1.25 cm. The measured depth is 1.0 ± 0.1 mm. The difference in depth is roughly 20 percent, which is excellent.

It is also interesting to note pressure and plastic strain-rate profiles in Figure 85 and Figure 86. Due to less difference in pressure magnitudes at 10 μs, this time is chosen to better represent the pressure distribution.

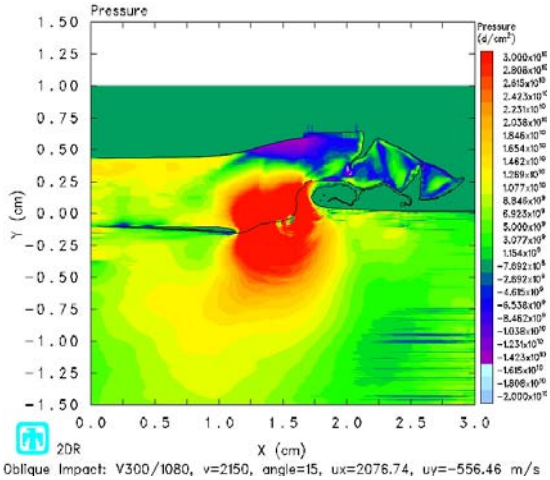

Figure 85 – Test #2 Pressure Profile, t=10.0 μs

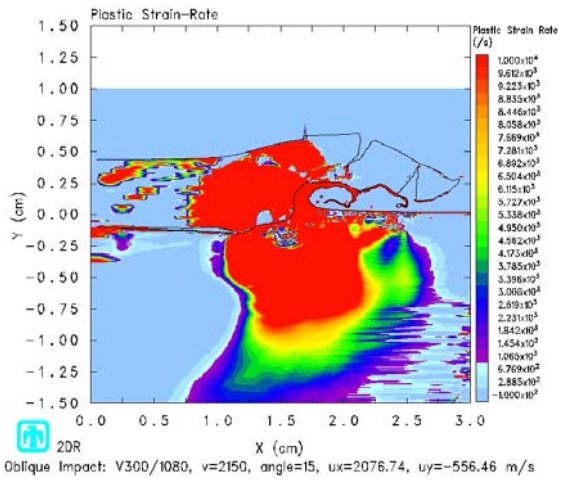

Figure 86 – Test #2 Strain Rate, t=10.0 μs

It is seen here that pressures on the order of 3.0 GPa and strain-rates as high as 10^4 /s are present. As with Test #1 and Test#4, this indicates that the plastic limit is exceeded and shock waves occur and that although the current Johnson-Cook strength model is fairly accurate, it has just exceeded its range of applicability.

Test #3 Simulation, v=2147 m/s @ 15°.

Figure 87 through Figure 89 show the simulation at interesting times of 2.5, 5.5, and 10.0 microseconds.

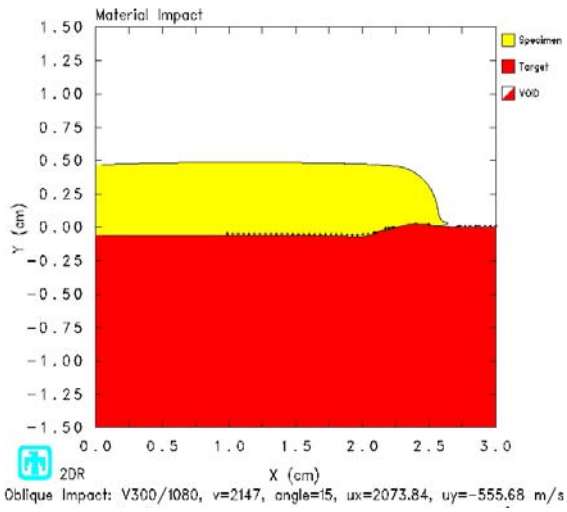

Figure 87 – Test #3 Sim, t=2.5 μs

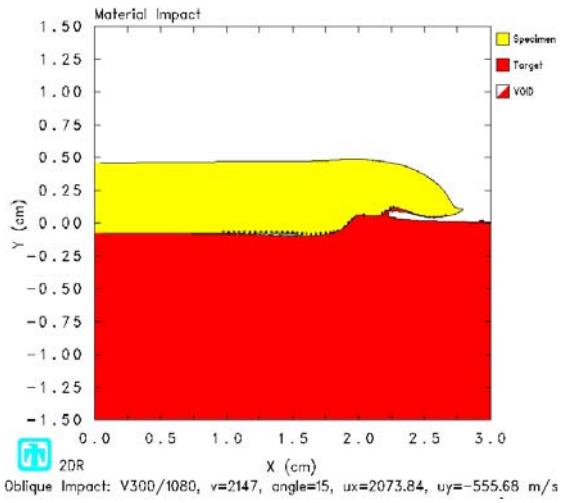

Figure 88 – Test #3 Sim, t=5.5 μs

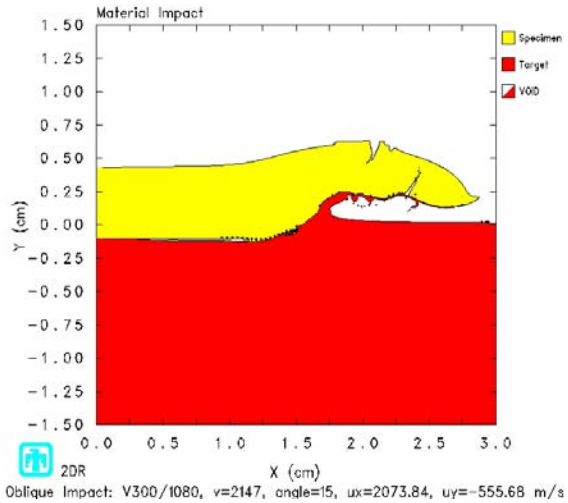

Figure 89 – Test #3 Sim, t=10.0 μs

As with Test #2, from 2.5 to 5.5 μs, the projectile and target start do deform and form a gouge. At 10 μs the projectile has formed two cracks, one on the top surface, and one on the bottom surface. The penetration depth of the target is roughly 1 cm. To determine a better estimate, Figure 90 shows a blown up image of the simulation at 10 μs. Note that the x and y axis scaling are different.

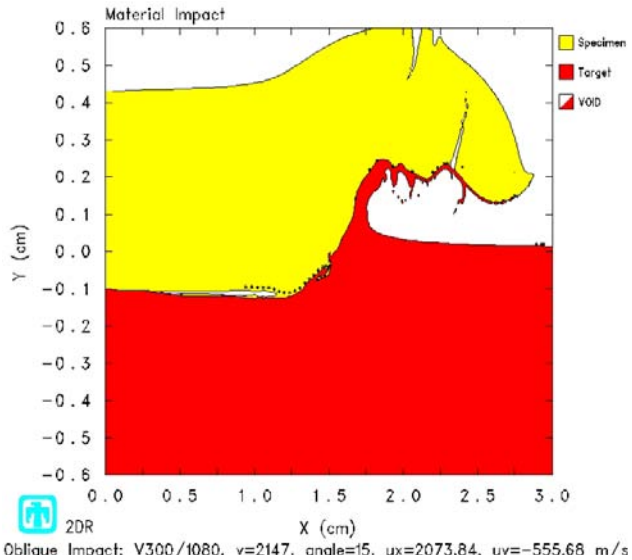

Figure 90 – Test #3 Sim, t=10.0 μs

It is seen that the simulated penetration depth is on the order of 1.15 cm. The measured depth is 1.0 ± 0.1 mm. The difference in depth is roughly 13 percent. Pressure and plastic strain-rate profiles are similar to Test #2 and are shown in Appendix C.

Bringing this altogether, Table 12 shows the comparison of the measured and simulated depths of the experiments.

Table 12 – Comparison of Experimental and CTH Results

Test	Velocity (m/s)	Angle (deg)	u_y (m/s)	Experiment Measured Depth (mm, ± 0.1 mm)	CTH Simulation Simulated Depth (mm)	Absolute Difference (mm)	Percent Difference
1	2225	10	386	0.5	0.7	0.2	29%
2	2150	15	556	1.0	1.25	0.25	20%
3	2147	15	556	1.0	1.15	0.15	13%
4	2163	10	376	0.5	0.7	0.2	29%

The results show that while CTH cannot fully capture the entire event in time, the current model does yield accurate results. With strain rates up to 10^4 /s, the use of the current strength model has exceeded its range of applicability.

Equivalent HHSTT Sled System

Using the methodology described earlier, the equivalent HHSTT can be developed using the Rod Impact results from Table 1. Test #1 is used to give the equivalent HHSTT sled system. It should be noted that only the velocity and angle of the equivalent system are affected by the different tests. Table 13 compares the two models side-by-side.

Table 13 – Model Comparison

Parameter	Rod Impact Model (Test #1)	Equivalent HHSTT Sled System
m (g)	4.78	2.00E+05
l (cm)	2.5	20.32
h (cm)	0.55	4.47
w (cm)	-	10.80
v (m/s)	2225	812.35
u_x (m/s)	2192.2	800.00
u_y (m/s)	-386.37	-141.10

It is worth mentioning here that this equivalent system doesn't exhibit typical HHSTT scenarios. The nominal HHSTT slipper height is 2.5 cm, whereas the equivalent

system height is 4.47 cm. This is due to the fact that the aspect ratio is constrained by the Buckingham Pi Theorem. Also, the nominal impact angle is roughly 0.03°, whereas the equivalent system impacts at 10°. Again, this is due to fact that the impact angle must remain the same between models.

Using the time scale of Equation 65, every 1 time unit of the Rod Impact model equals 22.3 time units of the equivalent HHSTT sled model. With the simulation of Test #1 running to 10 μs, the equivalent HHSTT sled model should be simulated out to 223 μs. Unfortunately, modeling this larger system out this far requires much more processing power than currently available here at AFIT. Because of this, the equivalent model is run out to only 10 μs. Figure 91 through Figure 93 show the displacement, pressure, and strain-rate profiles at 10 μs.

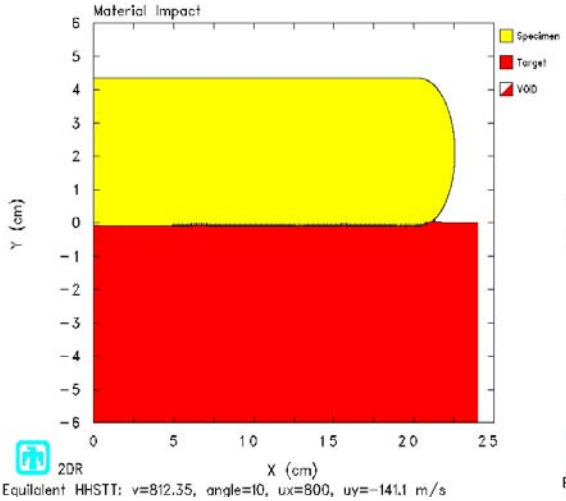

Figure 91 - Equivalent HHSTT Model, t=10 μs

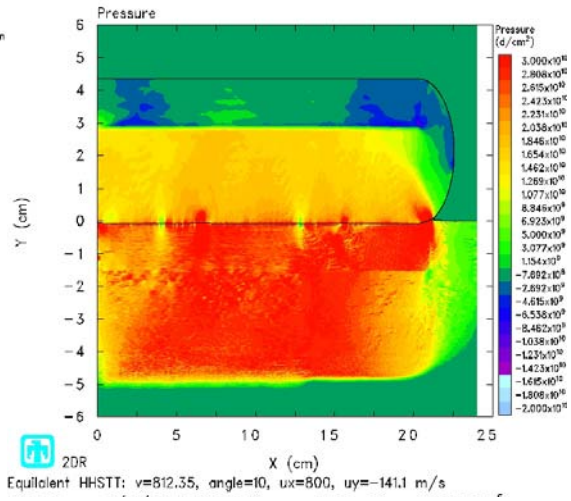

Figure 92 – Pressure, Equivalent Model, t=10 μs

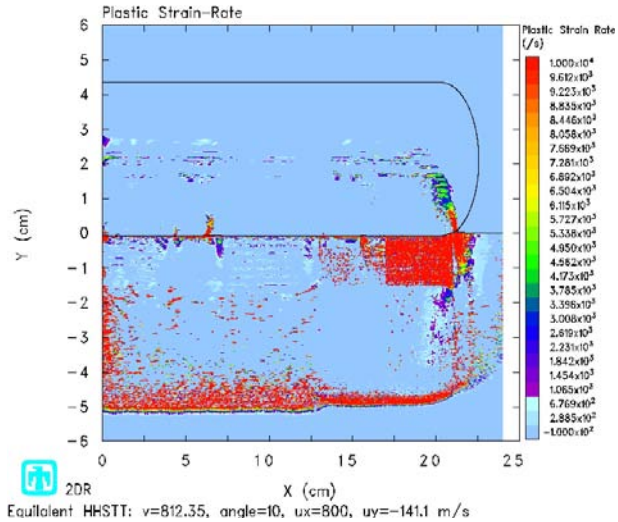

Figure 93 – Strain-Rate, Equivalent Model, t=10 μs

As can be seen, pressures of 3 GPa and strain-rates up to 10^4 /s are present just as in the Cinnamon simulations. Figure 94 shows a close-up of the impact zone, note the y-axis scaling.

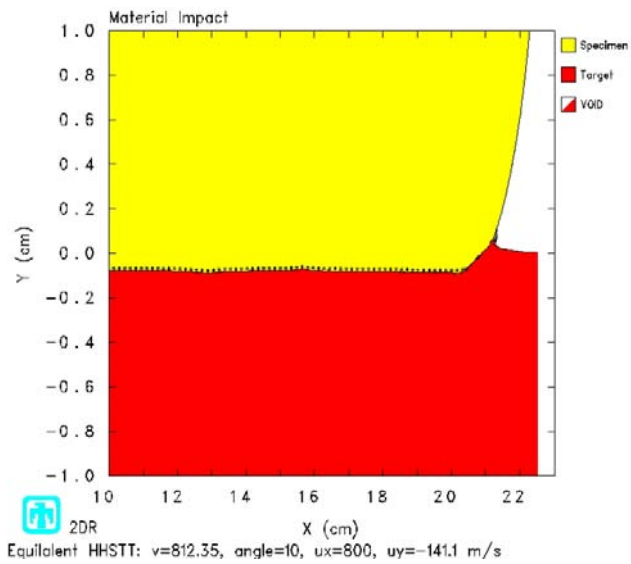

Figure 94 – Equivalent HHSTT Model, t=10 μs

As can be seen, the simulation the equivalent model predicts a penetration depth of roughly 1.0 mm at 10 μs. Although the CTH model cannot predict penetration depth beyond 10 μs, Figure 94 does show the initial signs of gouge formation through the high

pressure core and material interaction at the lower front area of the slipper, suggesting that the equivalent HHSTT sled system will eventually develop a classic gouge.

This suggests that although the test facilities here at AFIT are not capable of velocities in the realm of the HHSTT, it is possible to utilize these facilities to further the understanding of this gouging phenomenon. With the Buckingham Pi and CTH models producing good results, it is possible to relate the experiments made here to real sled systems at the HHSTT.

V. Conclusions and Recommendations

Conclusions

The primary goal of this research was to compare a computer simulation with experiment of an oblique ballistic impact. Through the Buckingham Pi Theorem, this model was scaled up to an equivalent HHSTT sled system. While this equivalent system does not physically exist, it did give ballpark estimates of what similar systems should experience under the same conditions as the experiments. The hydrocode computer program CTH was used to validate that it can simulate a cylindrical projectile impacting a target at an oblique angle using a plane-strain analysis; verify the experimental ballistic impacts; and to simulate the equivalent HHSTT sled model to see if the gouging phenomena were present. To reach the primary goal of this work, a series of model comparisons were made. The conclusions of this work are summarized in the following bullets.

- Through comparisons of CTH simulations of axisymmetric and plane-strain vertical impacts, it was shown that CTH can accurately simulate an axisymmetric impact event using a plane-strain analysis up to 10 μs. Pressure profiles

comparisons showed that they differ, but only by 15 to 30 percent at most in magnitude.

- It was shown that the predicted penetration depths are greater than the Cinnamon experiments by 13 to 29 percent, which is quite excellent. Pressures and strain rates of 3 GPa and 10^4 /s were observed. This shows that while the Johnson-Cook strength model was based on strain rates up to 10^3 /s, the current model is accurate.

- Through the use of dimensional analysis, an equivalent HHSTT sled system was developed based on Test #1 experiment. Unfortunately, modeling this larger system out to the required time required much more processing power than currently available. However, the simulation was run out to 10 μs, and showed signs of gouge initiation as in the early stages of the Cinnamon simulations.

- This suggests that although the test facilities here at AFIT are not capable of velocities in the realm of the HHSTT, it is possible to utilize these facilities to further the understanding of the gouging phenomenon. Since the Buckingham Pi and CTH models produced good results, it is possible to relate the experiments made here to real sled systems at the HHSTT.

Recommendations for Future Research

This investigation assumed, along with Szmerekovsky, Rickerd, and others, that the mass of the HHSTT sled system is evenly distributed over the four slippers, and that the slipper is oriented flat and level against the rail. While this may be a fairly good assumption when the sled is at rest, it is most likely not true at high velocities. Aerodynamic forces, rail characteristics, and sled dynamics can have profound effects on weight distribution and pitch angle. The validity of this assumption should be investigated.

The HHSTT has an epoxy coating on the rails, which serves as a type of lubricant to mitigate gouging. Neither metallurgical analysis on the experimental target rails nor effects of coatings was within the scope of this work. Addition of coatings to the CTH models would allow improved comparisons to the actual experiments. This, along with a

metallurgical analysis of the target rails, would enhance the understanding of the HHSTT gouging phenomena.

The Johnson-Cook coefficients used in this work was based on the prior work of Kennan and Yun. They utilized Split Hopkinson Bar tests in their analysis, which were only able to give data on strain rates up to 10^3 /s. However, strain rates on the order of 10^4 /s were seen in the CTH simulations. To more accurately define the strength models, other testing methods that are capable of yielding data on higher orders of magnitude of strain rates should be utilized, such as Flyer Plate tests.

The impact angles in the Cinnamon experiments were chosen two to three times the minimal angle required to theoretically gouge the rail. This was done to ensure gouging of the rail. However, it was shown that the higher the vertical velocity, the shorter the time frame CTH can simulate a cylindrical projectile impacting a target at an oblique angle using a plane-strain analysis. This resulted in CTH not being able to fully simulate the event in time. This also led to an equivalent HHSTT model with the same impact angle, which is not typically seen in the field. More impact experiments should be utilized with a compromise between matching impact angle and vertical kinetic energy, since it is difficult to match both at the same time here at AFRL.

Appendix A. CTH Input Deck of Axisymmetric – Plane Strain Comparison

```
*eor* genin

Axisymmetric Impact: V300 on 1080, v=375 m/s

control
  mmp
  ep
  vpsave
endcontrol

mesh
  block 1  geom=2dc    type=e   *  2dc is two dimensional cylindrical
                                *  e is for an Eulerian solution
    x0=0.0
      x1  n=60  w=0.6 dxf=0.01
      x2  n=8  w=0.4 dxf=0.05
      x3  n=20   w=2. dxf=0.1

    endx
    y0=-4.0
      y1  n=20  w=2 dyf=0.1
      y2  n=20  w=1 dyf=0.05
      y3  n=350 w=3.5 dyf=0.01
    endy
  endb
endmesh


insertion of material

   block 1
     package topblock
       material 1
       numsub 50
       yvel -375.e2     *  Change only the first number, leave 'e2'
                        *  this converts m/s to cm/s.
       insert box       *  This is where you input the cylinder -
                        *  only model 1/2 of cylinder, and then
                        *  "mirror" in plotting.
                        *  Format is p1 is the bottom center point of
                        *  cylinder.
                        *  p2 is top right hand corner of cylinder.
         p1 0.0   0.275 *  Change p1 and p2 to define the size of rod.
         p2 0.275 2.5
       endinsert

       delete circle
         center 0 0.275
         radius 0.275
       enddelete
```

```
     endpackage

     package tip           * Insert circular rod tip
       material 1
       numsub 50
         yvel -375.e2

       insert circle
         center 0 0.275
         radius 0.275
       endinsert

     endpackage

     package target       *  Insert Target
       material 2
       numsub 50
       insert box
         p1 0.0, 0.0
       p2 3, -4.0
       endinsert
     endpackage
  endblock
endinsertion

edit
  block1
  expanded
  endblock
endedit

tracer                    * Tracer Points
  add 0     0.01
  add 0     0.275
  add 0.275 0.01
  add 0.275 0.275
endt

eos
*  Information for metals
   MAT1 SES STEEL_V300             *  EOS for Vascomax 300 already in
CTH
   MAT2 SES IRON                   *  EOS for Iron should be close
enough for 1080
endeos

epdata
 mix 3
   matep 1 JO USER      * J-C coefficients for VascoMax 300.
      ajo= 2.17e10      * Dynes/cm^2
      bjo= 0.124e10     * Dynes/cm^2
      cjo= 0.0046
      mjo= 0.95
      njo= 0.3737
      tjo= .040161e-1
```

```
      poisson= 0.283

   matep 2 JO USER      * J-C coefficients for 1080 steel.
      ajo= 5.25e9       * Dynes/cm^2
      bjo= 3.59e7       * Dynes/cm^2
      cjo= 0.29
      mjo= 6.525e-1
      njo= 0.6677
      tjo= .1591885e-1
      poisson= 0.27

 vpsave
 lstrain
endep

****************************************************
*eor* cthin

Axisymmetric Impact: V300 on 1080, v=375 m/s
control
  mmp
  tstop = 15.0e-6     * you may need to increase the stop time to reach
                      * end of event.
endc

Convct
 convection=1
 interface=high_resolution
endc

fracts
 pfrac1 -2.4e10
 pfrac2 -1.38e10
 pfmix  -12.0e9
 pfvoid -12.0e9
endf

edit
  shortt
    tim 0.0,   dt = 1.0
  ends
  longt
    tim 0.0,   dt = 1.0
  endl
  plott
    tim 0.0    dt = 0.25e-6      * this sets the time step it plots at
                                 * 1/2 microsecond
  endp
  histt
   tim  0.0,   dt = 0.25e-6      * this sets the time step it plots at
                                 * 1/2 microsecond
   htracer all
  endh
ende
```

```
boundary
   bhy                          * Rigid boundaries all around
     bl 1
       bxb = 0 , bxt = 1
       byb = 1 , byt = 1
     endb
   endh
endb

celltherm o
 mmp3                  *  This was recommended by Eglin and appears
                       *  to give good results as well.
 ntbad 1000000
endc
```

Appendix B. CTH Input Deck for Rod Impact Test #1

```
*eor* genin

Oblique Impact: V300/1080, v=2225, angle=10, ux=2192.2, uy=-386.37 m/s

* All output from CTHgen will have this title.
*
* This is an impact scenario of a Vascomax 300 projectile
* hitting a 1080 steel target.
*
control
  mmp
  ep
  vpsave
endcontrol
*
*_____________________________________________________________________
*
mesh
  block 1  geom=2dr    type=e    * This section defines the mesh, not
                                 * the cylinder or block.
                                 * 2dr = 2D rectangle (plain strain) -
                                 * Use 2dc for axisymmetric.
                                 * e = Eulerian solution.

    x0=0.0                       * x0 = left starting value of x.
      x1  n=10 w=1.0  dxf=0.100  * x1,x2 = x subzone for defining
                                 * different meshes along x.
      x2  n=50 w=0.5  dxf=0.010  * ALL DIMENSIONS MUST BE IN cm!
      x3  n=220 w=1.1 dxf=0.005  * n = # of cells; w = section width;
      x4  n=40 w=0.4  dxf=0.010  * dxf = dx first; dxl = dx last
                                 * (optional)
      x5  n=20 w=2.0  dxf=0.100
    endx
    y0=-4.0                      * y has same inputs as x
      y1  n=20  w=2.0 dyf=0.10   * y0 = bottom starting position.
      y2  n=140 w=1.4 dyf=0.01
      y3  n=240 w=1.2 dyf=0.005
      y4  n=40  w=0.4 dyf=0.10
    endy
  endb
endmesh
*
*_____________________________________________________________________
*
insertion of material

   block 1
     package rod       * Insert rectangular rod and rotate
       material 1
       numsub 100
```

```
      xvel 2192.2e2    *  Change only the first number, leave 'e2'
                       *  this converts m/s to cm/s.
      yvel -386.37e2

      insert box        *  This is where you input the projectile.
         p1 0.0 0.0
         p2 2.225 0.55  *  Format: p1 = bottom center point of
                        *  cylinder.
                        *  p2 = top right hand corner of cylinder.
                        *  Change p1 and p2 to define the size of rod.
      endinsert

      delete circle   * Delete a circle for tip insertion (next step).
        center 2.225 0.275
        radius 0.275
      enddelete
    endpackage

    package tip           * Insert circular rod tip
      material 1
      numsub 100
      xvel 2192.2e2       * Separate package. Must include velocity.
      yvel -386.37e2

      insert circle
        center 2.225 0.275
        radius 0.275
      endinsert
    endpackage

    package target        * Insert Rail Material
      material 2
      numsub 100
      insert box
        p1 0.0 -4.0
      p2 5.0 0.0
      endinsert
    endpackage

  endblock
endinsertion
*
*_____________________________________________________________________
*
edit
  block1
  expanded
  endblock
endedit
*
*_____________________________________________________________________
*
eos                         * Eq Of State
```

```
   MAT1 SES STEEL_V300     * Sesame Eq of State tables, limited
                           * materialselection.
   MAT2 SES IRON           * Iron = closest material available to 1080.
endeos

epdata                   * Elastic/Plastic data
 mix 3                   * mix 3 = normalized vol avg yeild strength

   matep 1 JO USER       * J-C coefficients for VascoMax 300.
      ajo= 2.17e10       * Dynes/cm^2
      bjo= 0.124e10      * Dynes/cm^2
      cjo= 0.0046
      mjo= 0.95
      njo= 0.3737
      tjo= .040161e-1
      poisson= 0.283

   matep 2 JO USER       * J-C coefficients for 1080 steel.
      ajo= 5.25e9        * Dynes/cm^2
      bjo= 3.59e7        * Dynes/cm^2
      cjo= 0.29
      mjo= 6.525e-1
      njo= 0.6677
      tjo= .1591885e-1
      poisson= 0.27

 vpsave
 lstrain
endep

*
*_____________________________________________________________________
*
tracer
                * Tracer input, starting at x1,y1 to ending x2,y2.
                * n=number of tracers to distribute including
endpoints.
* Projectile boundary
  add 1.0 .01 to 3.0 .01 n=50
endt
*
*_____________________________________________________________________
*
*eor* cthin

Oblique Impact: V300/1080, v=2225, angle=10, ux=2192.2, uy=-386.37 m/s

control             * Defines sys parameters for execution.
  mmp               * mmp = multiple pressures and temps in mixed
                    * material cells.
  tstop = 15.0e-6   * tstop = Problem stop time in seconds.
  cpshift=600.      * cpshift allows extra time for CTH to right data.
endc
*
*_____________________________________________________________________
```

```
*
Convct                          * Convection control input.
 convection=1                   * Convect internal energy based on
                                * energy density and mass density.
                                * Discards kinetic energy.
 interface=high_resolution      * interface tracker, high_res
                                * recommended for 2D.
endc
*
*_____________________________________________________________________
*
fracts              * Fracture Strengh
 pfrac1=-2.4e10     * pfrac# = fracture pressure or stress of material #
 pfrac2=-1.38e10    * pfrac1 and 2 verified by J Cinnamon.
 pfmix=-12.0e9      * pfmix = fracture stress or pressure in cell with
                    * mixed mat no voids.
 pfvoid=-12.0e9     * pfvoid = fracture press or stress in cell with
                    * void.
endf
*
*_____________________________________________________________________
*
edit
  shortt
    tim 0.0, dt=1.0       * Restart data will be written every 'dt'
                          * seconds.
  ends

  longt
    tim 0.0, dt=1.0       * Restart data will be written every 'dt'
  endl

  plott
    tim 0.0 dt=0.25e-6     * cthplot data is written to restart file
                           * every 'dt' seconds starting at 'tim'.
  endp                     * Beware - Restart file size limited to 2GB.

  histt
    tim 0.0 dt=0.25e-6    * History data will be written to hcta every
    htracer all           * 'dt' seconds.  Data will be written for all
                          * tracer points.
  endh

ende
*
*_____________________________________________________________________
*
boundary
   bhy                            * rigid boundaries all around
     bl 1
       bxb = 1, bxt = 1
       byb = 1, byt = 1
     endb
   endh
endb
```

```
*
*_____________________________________________________________________
*
vadd                                * Apply vel to keep gouge in mesh
  block=1
  tadd=0.0
  xvel=-2192.2e2
endvadd
*
*_____________________________________________________________________
*
celltherm o
 mmp3                   *  This was recommended by Eglin and appears
                        *  to give good results as well.
 ntbad 1000000
endc
*
*_____________________________________________________________________
*
```

Appendix C. CTH Plots of Cinnamon Simulations

Test #4:

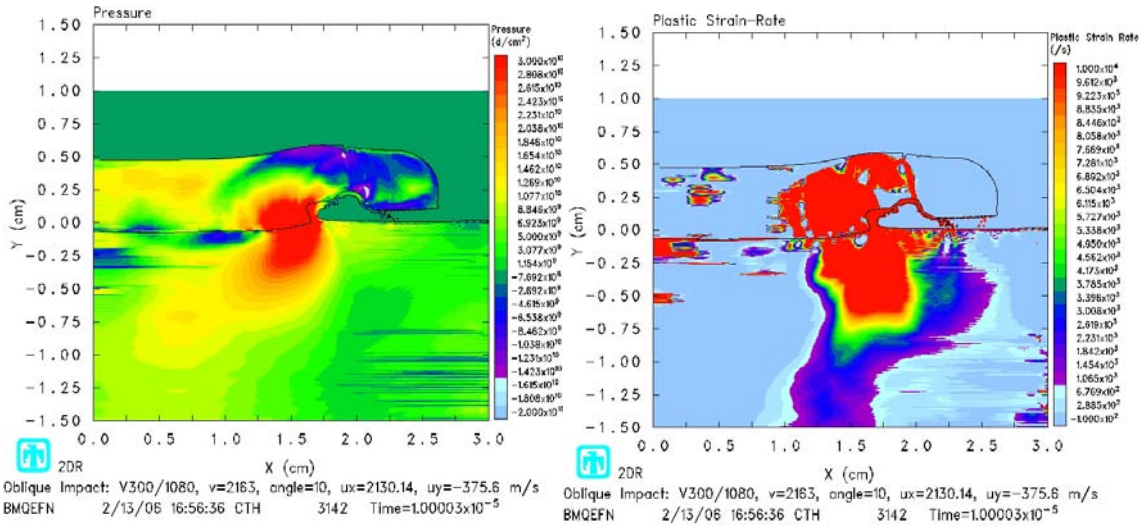

Test #3:

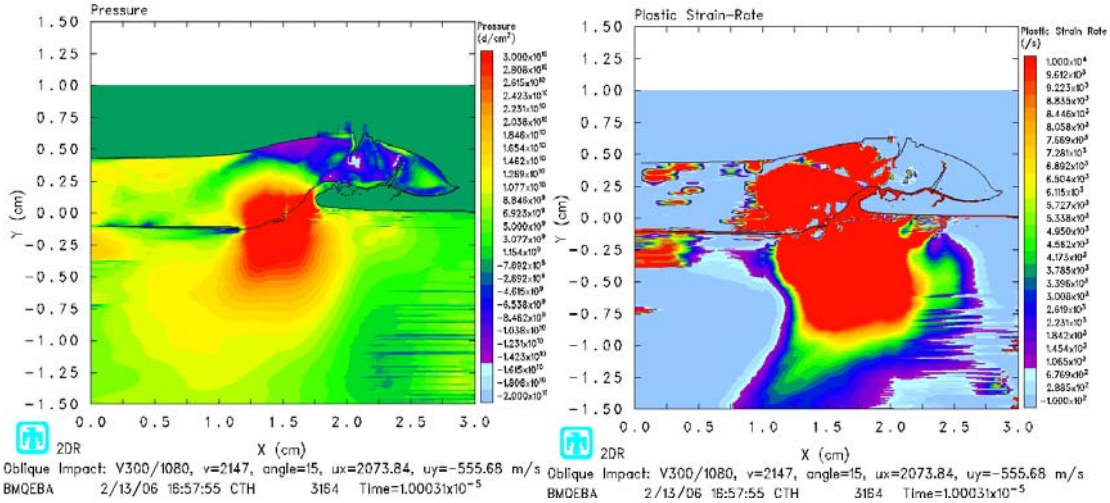

Bibliography

1. Hooser, Michael. "Simulation of a 10,000 Foot per Second Ground Vehicle." *21st AIAA Advanced Measurement Technology and Ground Testing Conference.* Number AIAA 2000-2290. Denver CO: AIAA, 2000.

2. Laird, David J. *The Investigation of Hypervelocity Gouging AFIT/DS/ENY 02-01*. PhD dissertation, Air Force Institute of Technology, Wright-Patterson AFB OH, March 2002.

3. Laird, D., and Palazotto, A., 2004. "Gouge Development During Hypervelocity Sliding Impact". *International Journal of Impact Engineering*, 30, pp. 205-223.

4. Szmerekovsky, Andrew G. *The Physical Understanding of the use of Coatings to Mitigate Hypervelocity Gouging Considering Real Test Sled Dimensions AFIT/DS/ENY 04-06*. PhD dissertation, Air Force Institute of Technology, Wright-Patterson AFB OH, September 2004.

5. Szmerekovsky, Andrew G., Palazotto, A. N., Baker W. P. "Scaling Numerical Models for Hypervelocity Test Sled Slipper-Rail Impacts". *International Journal of Impact Engineering*, Vol. 32, No. 6, 2006.

6. Rickerd, Gregory S. *An Investigation of a Simplified Gouging Model*. MS thesis, AFIT/GAE/ENY/05-M19. School of Engineering and Management, Air Force Institute of Technology (AU), Wright-Patterson AFB OH, March 2005.

7. Nicholas, Theodore and Rodney F. Recht. *High Velocity Impact Dynamics*, chapter 1 Introduction to Impact Phenomena, 1-63. New York NY: John Wiley and Sons., 1990.

8. Nicholas, Theodore. *Impact Dynamics*, chapter 4 Elastic-Plastic Stress Waves, 95-154. Malabar FL: Krieger Publishing Company., 1982.

9. Nicholas, Theodore. Class Handout, AERO 899, High Velocity Impact. School of Engineering and Management, Air Force Institute of Technology, Wright-Patterson AFB OH, Fall Quarter 2004.

10. Zukas, Jonas A. *Introduction to Hydrocodes*, San Diego CA: ELSEVIER Inc., 2004.

11. Anderson, Charles F. "An Overview of the Theory of Hydrocodes," *International Journal of Impact Engineering*, 5:33-59 (1987).

12. Nicholas, Theodore and Rodney F. Recht. *High Velocity Impact Dynamics*, chapter 3 Material Characterization at High Strain Rates, 127-279. New York NY: John Wiley and Sons., 1990.

13. Çengel, Yungas A, and Cimbala, John M. *Fluid Mechanics : Fundamentals and Applications*, Boston: McGraw-Hill, 2006.

14. Cinnamon, J. D. and Palazotto, A. N. "Validation of a General Approximation for Impact Penetration Depth Considering Hypervelocity Gouging Data" Submitted for Publication, Proceedings of the ASME Pressure Vessel and Piping Conference, Paper PVP2006-ICPVT11-93584, July 23-27, 2006.

15. McGlaun, J.M., et al. "CTH: A Three-dimensional Shock Wave Physics Code," *International Journal of Impact Engineering*, 10: 351-360 (1990).

16. Kennan Zachary A. Determination of the Constitutive Equations of 1080 Steel and VascoMax 300. MS thesis, AFIT/GAE/ENY/05-J05. School of Engineering and Management, Air Force Institute of Technology (AU), Wright-Patterson AFB OH, June 2005.

17. Yun, Su-Jin, Palazotto, A., Cinnamon, J. D., "Temperature Dependent Johnson-Cook Type Visco-Plastic Constitutive Model for Vascomax 300 and 1080 Steel and Plastic Deformation Behavior" Submitted for Publication, *Journal of Mechanics of Materials*.

18. Nguyen, Minh C. *Analysis of Computational Methods for the Treatment of Material Interfaces*. MS thesis, AFIT/GAE/ENY/05-M15. School of Engineering and Management, Air Force Institute of Technology (AU), Wright-Patterson AFB OH, March 2005.

19. Nguyen, M. C., Palazotto, A. N., and Cinnamon, J.D., 2005. "Analysis of Computational Methods for the Treatment of Material Interfaces". 46th AIAA/ASME/ASCE/AHS/ASC Structures, Structural Dynamics, and Materials Conference, Austin, TX, 18-21 April, AIAA.

REPORT DOCUMENTATION PAGE

Form Approved
OMB No. 074-0188

The public reporting burden for this collection of information is estimated to average 1 hour per response, including the time for reviewing instructions, searching existing data sources, gathering and maintaining the data needed, and completing and reviewing the collection of information. Send comments regarding this burden estimate or any other aspect of the collection of information, including suggestions for reducing this burden to Department of Defense, Washington Headquarters Services, Directorate for Information Operations and Reports (0704-0188), 1215 Jefferson Davis Highway, Suite 1204, Arlington, VA 22202-4302. Respondents should be aware that notwithstanding any other provision of law, no person shall be subject to an penalty for failing to comply with a collection of information if it does not display a currently valid OMB control number.
PLEASE DO NOT RETURN YOUR FORM TO THE ABOVE ADDRESS.

1. REPORT DATE *(DD-MM-YYYY)*	2. REPORT TYPE	3. DATES COVERED *(From – To)*
17-03-2006	Master's Thesis	Aug 2004 – Mar 2006

4. TITLE AND SUBTITLE

Validation of a Scaled Plane Strain Hypervelocity Gouging Model

5a. CONTRACT NUMBER

5b. GRANT NUMBER

5c. PROGRAM ELEMENT NUMBER

6. AUTHOR(S)

Pendleton, Ronald J., Captain, USAF

5d. PROJECT NUMBER

5e. TASK NUMBER

5f. WORK UNIT NUMBER

7. PERFORMING ORGANIZATION NAMES(S) AND ADDRESS(S)

Air Force Institute of Technology
Graduate School of Engineering and Management (AFIT/EN)
2950 Hobson Way, Building 640
WPAFB OH 45433-8865

8. PERFORMING ORGANIZATION REPORT NUMBER

AFIT/GAE/ENY/06-M26

9. SPONSORING/MONITORING AGENCY NAME(S) AND ADDRESS(ES)

Dr. Neal Glassman, AFOSR (AFRL)
4015 Wilson Blvd, Room 713
Arlington, VA 22203-1954

10. SPONSOR/MONITOR'S ACRONYM(S)

11. SPONSOR/MONITOR'S REPORT NUMBER(S)

12. DISTRIBUTION/AVAILABILITY STATEMENT

APPROVED FOR PUBLIC RELEASE; DISTRIBUTION UNLIMITED.

13. SUPPLEMENTARY NOTES

14. ABSTRACT

The phenomenon of high speed impact is of great interest to the Air Force Office of Scientific Research and the Air Force Research Laboratory's Holloman High Speed Test Track. Rocket sled tests at the facility frequently are limited to velocities lower than actually attainable due to damage to the rail in the form of gouges. Direct observation of this gouging phenomenon is not currently possible. This leaves computational modeling as the only means to study the phenomenon. A computer model has previously been used to model the development of gouging at the Holloman High Speed Test Track. However, this model has not been experimentally verifiable due to its complexity.

This research is primarily concerned with comparing experiment and analysis of a simplified gouging model. This simplified gouging experiment utilized a 30 mm powder gun to shoot cylindrical projectiles at a target at oblique angles. Computer simulations of the event overestimated penetration depths by 13 to 29 percent, which is well within acceptable limits.

Using dimensional analysis, the simplified gouging model was scaled up to an equivalent sled system model. While this equivalent system does not actually exist, it does give reasonable estimates for similar sized systems.

15. SUBJECT TERMS

Hypervelocity Gouging, High Energy Impact, Impact, Impact Tests, Shock Waves

16. SECURITY CLASSIFICATION OF:			17. LIMITATION OF ABSTRACT	18. NUMBER OF PAGES	19a. NAME OF RESPONSIBLE PERSON
a. REPORT	b. ABSTRACT	c. THIS PAGE			Dr. A.N. Palazotto, USAF
U	U	U	UU	99	19b. TELEPHONE NUMBER *(Include area code)* (937) 255-3636 x4599 (anthony.palazotto@afit.edu)

Standard Form 298 (Rev. 8-98)
Prescribed by ANSI Std. Z39-18